LAWRENCE
LIVERMORE
NATIONAL
LABORATORY

LLNL-JRNL-836804

Titanium and chromium isotopic compositions of calcium-aluminum-rich inclusions: Implications for the sources of isotopic anomalies and the formation of distinct isotopic reservoirs in the early Solar System

Z. A. Torrano, G. A. Brennecka, C. M. Mercer, S. J. Romaniello, V. K. Rai, R. R. Hines, M. Wadhwa

June 28, 2022

Geochimica et Cosmochimica Acta

Disclaimer

Titanium and chromium isotopic compositions of calcium-aluminum-rich inclusions: Implications for the sources of isotopic anomalies and the formation of distinct isotopic reservoirs in the early Solar System

Zachary A. Torrano[a,1], Gregory A. Brennecka[b], Cameron M. Mercer[a,2], Stephen J. Romaniello[a], Vinai K. Rai[a], Rebekah R. Hines[a], Meenakshi Wadhwa[a]

[a]School of Earth and Space Exploration, Arizona State University, Tempe, AZ, 85287
[b]Lawrence Livermore National Laboratory, Livermore, CA, 94550

Corresponding Author: Zachary A. Torrano (ztorrano@carnegiescience.edu)

[1]Present address: Earth and Planets Laboratory, Carnegie Institution for Science, Washington, DC, 20015

[2]Present address: Geology, Geophysics, and Geochemistry Science Center, United States Geological Survey, Denver, CO, 80225

ABSTRACT

As the earliest-dated solids in our Solar System, calcium-aluminum-rich inclusions (CAIs) provide a record of their formation environment near the young Sun and hold clues to the formation of planetary-scale isotopic reservoirs in the solar protoplanetary disk. Although CAIs from several CV, CK, CM, CO, and ordinary chondrites have been analyzed previously for their Ti isotopic compositions, CAIs from just three CV chondrites have been analyzed for their Cr isotopic compositions, and only a handful of CAIs have been measured for both their Ti and Cr isotopic compositions. We report mass-independent Ti and Cr isotopic anomalies in several CAIs from CV and CK chondrites; this is the first report of the Cr isotopic composition of a CAI from a CK chondrite. With these additional data, we aim to better constrain the compositional range of CAIs in ε^{50}Ti versus ε^{54}Cr space, thereby facilitating the isotopic characterization of the material inherited by the solar protoplanetary disk and the role of CAIs in the formation of distinct planetary-scale isotopic reservoirs in our early Solar System. The narrow range in isotopic anomalies in CAIs when compared to other early-formed refractory inclusions such as platy hibonite crystals (PLACs) and spinel-hibonite inclusions (SHIBs) suggests that CAIs record the mixing of these precursor materials and the averaging of their larger isotopic anomalies. The isotopic composition of CAIs is therefore likely the result of a combination of factors, including mixing of material inherited from their formation region, heterogeneous carrier phase distribution, and thermal processing in the disk. The ε^{50}Ti and ε^{54}Cr isotopic compositions of CAIs are not correlated, further demonstrating that these isotopic anomalies have different carrier phases. The Ti and Cr isotopic compositions of CAIs additionally show that CAIs alone cannot be responsible for the compositional difference between the non-carbonaceous chondritic (NC) and carbonaceous chondritic (CC) isotopic reservoirs but nevertheless do play a role in the formation of these large-scale isotopic reservoirs in the early Solar System.

1. INTRODUCTION

Calcium-aluminum-rich inclusions (CAIs) are highly refractory objects found in chondritic meteorites and are the earliest-dated solids to form in the Solar System at ~4.567 Ga (e.g., Amelin et al., 2010; Connelly et al., 2012). In addition to ancient absolute ages from Pb-Pb chronometry, most CAIs exhibit an inferred initial $^{26}Al/^{27}Al$ ratio of $\sim 5 \times 10^{-5}$, suggesting that these objects formed during a short time interval of less than 200,000 years (Jacobsen et al., 2008; MacPherson et al., 2012; Kawasaki et al. 2019; Liu et al., 2019). As such, CAIs record a snapshot of the earliest stages of the isotopic evolution of the Solar System and provide important constraints on protoplanetary disk dynamics. Previous studies have shown that CAIs record mass-independent isotope anomalies in most elements (e.g., Dauphas and Schauble, 2016; Burkhardt et al. 2019). Whereas the isotopes of certain elements show mass-independent variability that is resolvable at ε-level (parts per ten thousand deviation from a standard), others do not. The characterization of these isotopic anomalies is an important step towards constraining the nucleosynthetic processes that produced the ingredients of the solar protoplanetary disk as well as the mixing processes that occurred during the early evolution of our Solar System. Isotopic anomalies in the Fe-peak elements ($22 \leq Z \leq 30$) are of particular importance because their nucleosynthetic origin in the late evolution of massive stars and supernovae aid in identifying potential contributions from such sources to the early Solar System.

The mass-independent variations in the Ti and Cr isotopic compositions of meteorites have previously been utilized as tracers of Solar System dynamics and evolution (e.g., Trinquier et al., 2007, 2008, 2009; Qin et al., 2010; Warren, 2011). The neutron-rich isotopes of these two elements, ^{50}Ti and ^{54}Cr, are particularly useful because they are produced in variable amounts in Type Ia, Type II, and electron-capture supernovae (e.g., Rauscher et al., 2002; Woosley et al., 2002; Wanajo et al., 2013) and can be used to trace the inheritance of materials from these sources into the early Solar System, the distribution of these materials in the solar protoplanetary disk, and the genetic relationships between meteorite parent bodies. An isotopic dichotomy between “non-carbonaceous” (NC) and “carbonaceous” (CC) meteorites was recognizedin several isotope systems, including Ti and Cr (e.g., Warren, 2011). These distinct isotopic compositions are suggested to represent distinct reservoirs in the inner (NC) and outer (CC) Solar System that were likely isolated from each other by the formation and growth of Jupiter (Kruijer et al., 2017). This isotopic dichotomy may reflect the changing nature of material infalling from the parent molecular

cloud (e.g., Burkhardt et al., 2019; Nanne et al., 2019) as well as thermal processing (Trinquier et al., 2009), transport, and mixing occurring within the protoplanetary disk. In models suggesting that the isotopic dichotomy records a changing of the isotopic composition of infalling material, CAIs are considered to record the isotopic composition of the earliest stage of infall (Burkhardt et al., 2019; Nanne et al., 2019; Brennecka et al. 2020). Additional work has suggested that CAIs play a key role in the formation of the NC and CC reservoirs as well as the distinct CC meteorite compositions (e.g., Trinquier et al., 2009; Bryson and Brennecka, 2021). Thus, CAIs hold important clues to the formation of distinct isotopic reservoirs in the early Solar System and the processes that led to the distinctive isotopic compositions of different meteorite parent bodies.

In addition to the more abundant "normal" CAIs that are the focus of this study (referred to simply as CAIs from hereon), chondritic meteorites contain a variety of other refractory components such as platy hibonite crystals (PLACs) and spinel-hibonite inclusions (SHIBs). These rare and small objects have large and variable nucleosynthetic anomalies and typically also have lower than canonical $^{26}Al/^{27}Al$. These characteristics have been interpreted together to suggest that these rare objects represent the first generation of refractory matter in the early Solar System that formed prior to CAIs (e.g., Sahijpal and Goswami, 1998; Kööp et al., 2016a). In the case of $\varepsilon^{50}Ti$ values, CAIs exhibit a narrow range of ~20 (Heydegger et al., 1979; Niederer et al., 1980, 1981, 1985; Niemeyer and Lugmair, 1981, 1984; Loss et al., 1994; Chen et al., 2009; Leya et al., 2009; Trinquier et al., 2009; Williams et al., 2016; Simon et al., 2017; Davis et al., 2018; Ebert et al., 2018; Burkhardt et al., 2019; Render et al., 2019; Torrano et al., 2019; Shollenberger et al., 2022), while SHIBs have a range of ~200 (Ireland et al., 1990; Sahijpal et al., 2000; Liu et al., 2009; Kööp et al., 2016b) and PLACs have a range of >3000 (Ireland et al., 1990; Sahijpal et al., 2000; Liu et al., 2009; Kööp et al., 2016a); no Cr isotope data have been reported as yet for SHIBs and PLACs to our knowledge. Fractionation and Unidentified Nuclear effect (FUN) CAIs also have non-canonical $^{26}Al/^{27}Al$ and large $\varepsilon^{50}Ti$ and $\varepsilon^{54}Cr$ anomalies, but their high degree of mass-dependent fractionation complicates the interpretation of whether they formed prior to CAIs (as suggested for PLACs and SHIBs) or whether they formed after ^{26}Al had decayed. Even larger isotopic anomalies in ^{50}Ti and ^{54}Cr are recorded in presolar grains, which are likely the initial carriers of these isotopic anomalies (e.g., Dauphas et al., 2010; Qin et al., 2011; Gyngard et al., 2018; Nittler et al., 2018). It is possible that the large isotopic anomalies recorded by PLACs, SHIBs, and

presolar grains are related to those recorded by CAIs, perhaps through mixing processes and averaging of their initially large isotopic anomalies.

Although CAIs from several CV, CK, CM, CO, and ordinary chondrites have been analyzed for their Ti isotopic compositions (Heydegger et al., 1979; Niederer et al., 1980, 1981, 1985; Niemeyer and Lugmair, 1981, 1984; Loss et al., 1994; Chen et al., 2009; Leya et al., 2009; Trinquier et al., 2009; Williams et al., 2016; Simon et al., 2017; Davis et al., 2018; Ebert et al., 2018; Burkhardt et al., 2019; Render et al., 2019; Torrano et al., 2019; Shollenberger et al., 2022), only CAIs from CV chondrites have been analyzed for their Cr isotopic compositions (Birck and Allègre, 1984, 1985; Papanastassiou, 1986; Birck and Lugmair, 1988; Loss et al., 1994; Trinquier et al., 2007). Additionally, the vast majority of the CAIs measured for either their Ti or Cr isotopic compositions are from Allende. It is noted that CV3 chondrites, particularly Allende, are known to have been altered extensively by secondary processes on their parent body (e.g., Krot et al., 1998). Furthermore, only a few CAIs from the Allende and Vigarano CV3 chondrites have been measured for both their Ti and Cr isotopic compositions. Therefore, it is important to measure both the Ti and Cr isotopic compositions of CAIs from multiple non-Allende chondritic meteorites to evaluate the compositional range of CAIs in ε^{50}Ti versus ε^{54}Cr space, the origins of material inherited by the solar protoplanetary disk, the relationship between the isotopic compositions of CAIs and other refractory inclusions such as PLACs and SHIBs, and the role of CAIs in the formation of the planetary-scale isotopic dichotomy in the early Solar System. In this work, we report the mass-independent variations in the Ti and Cr isotopic compositions of 11 CAIs from several CV chondrites and a CK chondrite; the Ti isotopic compositions of 6 of these CAIs were previously reported in Torrano et al. (2019).

2. SAMPLES AND METHODS

2.1. Sample Description and Extraction

The sample set studied here includes ten CAIs from six CV chondrites, including oxidized ($CV3_{ox}$) and reduced ($CV3_{red}$) subgroups, and one CAI from a CK chondrite. The Ti isotopic compositions of six of these CAIs were reported previously by Torrano et al. (2019): ZT1 and ZT2 from $CV3_{red}$ Leoville, ZT3 from $CV3_{ox}$ Northwest Africa (NWA) 6991, ZT5 from $CV3_{ox}$ NWA 7891, and ZT7 and ZT8 from $CV3_{ox}$ NWA 3118. Five new CAIs were obtained for this work: ZT6 from NWA 2900 (originally classified as a CV3, but reclassified as a CK3 by Torrano et al., 2020),

ZT10 from $CV3_{ox}$ NWA 6991, ZT13 and ZT14 from $CV3_{ox}$ Axtell, and Saguaro from $CV3_{red}$ NWA 5508. A summary of the characteristics of these samples is shown in Table 1. All sample handling was conducted in the Isotope Cosmochemistry and Geochronology Laboratory (ICGL) at Arizona State University (ASU). The extraction of CAIs ZT1, ZT2, ZT3, ZT5, ZT7, and ZT8 was described by Torrano et al. (2019) and the CAIs ZT6, ZT10, ZT13, ZT14, and Saguaro—data for which are reported here for the first time—were extracted following the same procedures.

Table 1. List of the CAIs included in this study.

CAI	Meteorite	Mass Extracted (mg)	CAI Type	REE Pattern
ZT1	Leoville ($CV3_{red}$)	18.7	CG, B1	Group I
ZT2	Leoville ($CV3_{red}$)	4.7	CG, B1	Group II
ZT3	NWA 6991 ($CV3_{ox}$)	8.7	FG	Group II
ZT5	NWA 7891 ($CV3_{ox}$)	3.0	CG	Group II
ZT6	NWA 2900 (CK3)	30.5	CG	Group I
ZT7	NWA 3118 ($CV3_{ox}$)	5.7	CG, CTA	Group I
ZT8	NWA 3118 ($CV3_{ox}$)	5.8	CG, CTA	Group III
ZT10	NWA 6991 ($CV3_{ox}$)	7.0	FG	Group II
ZT13	Axtell ($CV3_{ox}$)	20.2	CG	Group I
ZT14	Axtell ($CV3_{ox}$)	24.4	FG	Group II
Saguaro	NWA 5508 ($CV3_{red}$)	220.3	CG, B2	Group I

$CV3_{ox}$ = CV3 oxidized subgroup; $CV3_{red}$ = CV3 reduced subgroup; CG = coarse-grained; FG = fine-grained; CTA = compact type A.

2.2. Analytical Methods

2.2.1 Sample Digestion and Concentration Measurements

Following extraction, the CAI samples were powdered using a clean agate mortar and pestle. Samples were first treated with a 3:1 ratio of concentrated HF and HNO_3 on a hot plate for ~48 hours, dried down, and then digested in Parr bombs in a 2:1 ratio of concentrated HF and HNO_3 at 190 ºC for >96 hours. Following Parr bomb digestion, samples were dried down and then brought into solution in 6N HCl followed by 3% HNO_3. An aliquot of ~5% of each sample solution was reserved for elemental concentration measurements using the Thermo Scientific iCAP-Q quadrupole inductively coupled plasma mass spectrometer in the Metals, Environmental and Terrestrial Analytical Laboratory (METAL) at ASU. Aliquots of the remaining ~95% of the sample solutions were then processed for Ti and Cr purification (see below). Similar digestion procedures were used for the terrestrial rock standards BCR-2 and AGV-1 and the Smithsonian Allende reference powder (i.e., a powdered and homogenized bulk sample of the Allende CV chondrite obtained from the Smithsonian National Museum of Natural History). Based on repeated

analyses of standards, we estimate an uncertainty (2SD) of ±5% for elemental concentration measurements.

2.2.2 Titanium Purification and Isotopic Analyses

An aliquot (equivalent to ~7–12 μg Ti) of the sample solution for each CAI was chemically processed for purification of Ti in the ICGL at ASU following the methods of Torrano et al. (2019). The Ti yields exceeded 95% for all samples and standards with a total procedural blank of <10 ng of Ti, which is insignificant compared to the total amount of Ti in the sample aliquots processed for Ti purification.

The mass spectrometry protocols used for Ti isotopic measurements of six of the CAIs included in this study were previously reported by Torrano et al. (2019). Titanium isotopic measurements of the five additional CAIs included in this study were conducted using the Thermo Neptune multicollector inductively coupled plasma mass spectrometer (MC-ICPMS) at ASU using a jet sample cone and an H-skimmer cone in high-resolution mode (i.e., with a mass resolving power >8000). Samples were introduced via a Cetac Aridus II desolvating nebulizer attached to a self-aspirating PFA with an uptake rate of 100 μL/min. An uptake time of 90 s and a wash time between consecutive sample and standard measurements of 120 s were used. Each run for a sample, standard, or blank comprised 50 cycles with an 8 s integration time per cycle. Purified Ti samples and standards were analyzed at a concentration of 1 ppm, and the typical sensitivity resulted in a ^{48}Ti signal of ~25V (using a $10^{11}\Omega$ resistor on the Faraday cup). Data were collected by switching between two different cup configurations: The intensities of ^{44}Ca, ^{46}Ti, ^{47}Ti, ^{48}Ti, and ^{49}Ti were measured in the first cup configuration, followed by measurement of ^{47}Ti, ^{49}Ti, ^{50}Ti, ^{51}V, and ^{52}Cr intensities with the second cup configuration. Intensities of ^{44}Ca, ^{51}V, and ^{52}Cr were used to correct for isobaric interferences on the Ti masses. All data reduction was performed offline.

Mass-independent titanium isotopic compositions are reported relative to the NIST 3162a Ti standard after correction for instrumental and natural mass-dependent fractionation using sample-standard bracketing and internal normalization to ^{49}Ti/^{47}Ti applying an exponential mass fractionation law and a ^{49}Ti/^{47}Ti ratio of 0.749766 (Niederer et al., 1981). Titanium isotope anomalies are reported in ε notation, as defined below:

178 $$\varepsilon\,^{x}Ti = \left[\frac{\left({}^{x_{Ti}}/_{47_{Ti}}\right)_{sample}}{\left({}^{x_{Ti}}/_{47_{Ti}}\right)_{standard}} - 1\right] * 10^{4}$$

179 Where x is mass 46, 48, or 50 and ratios have been internally normalized.

180 To assess the accuracy and precision of our methodology for Ti isotope analyses (including
181 chemical separation and mass spectrometry), we purified and measured Ti isotopes in the BCR-2
182 and AGV-1 terrestrial rock standards and the Smithsonian Allende reference powder alongside
183 samples. Our external reproducibility (2SD) based on repeat measurements of pure synthetic Ti
184 standards as well as terrestrial and Allende meteorite rock standards in our laboratory is ± 0.17 for
185 ε^{46}Ti, ± 0.07 ε^{48}Ti, and ± 0.17 for ε^{50}Ti (2SD) (see Fig. 2 in Torrano et al., 2019).
186
187 **2.2.3 Chromium Purification and Isotopic Analyses**
188 An aliquot (equivalent to ~1.5–6 μg Cr) of the sample solution for each CAI was
189 chemically processed for purification of Cr in the ICGL at ASU following the methods described
190 by Torrano et al. (2021). The Cr yields of all samples and standards exceeded 90% with an average
191 total procedural blank of less than 2 ng of Cr, which is insignificant compared to the total amount
192 of Cr in the sample aliquots processed for Cr purification. Prior to isotope measurements, ^{56}Fe/^{52}Cr
193 $< 5\times10^{-4}$ was ensured in the purified Cr solutions for all samples and standards to avoid any effect
194 of the isobaric interference of ^{54}Fe on ^{54}Cr (Torrano et al., 2021).
195 Chromium isotopic measurements were conducted on a Thermo Neptune MC-ICPMS at
196 ASU using a jet sample cone and an H-skimmer cone in high-resolution mode. Samples were
197 introduced through an Elemental Scientific Apex-Q desolvating system attached to a self-
198 aspirating PFA with an uptake rate of 100 μL/min. An uptake time of 90 s and a wash time between
199 consecutive sample and standard measurements of 120 s were used. Each run for a sample,
200 standard, or blank comprised 36 cycles with an 8 s integration time per cycle. Purified Cr samples
201 and standards were analyzed at a concentration of 800 ppb, and the typical sensitivity for ^{52}Cr was
202 ~25V (using a $10^{11}\Omega$ resistor on the Faraday cup). The intensities of ^{50}Cr, ^{52}Cr, ^{53}Cr, and ^{54}Cr were
203 measured, along with ^{49}Ti, ^{51}V, and ^{56}Fe to monitor and correct for isobaric interferences. All data
204 reduction was performed offline.
205 Mass-independent Cr isotopic compositions are reported relative to the SRM 979 Cr
206 standard after correction for instrumental and natural mass-dependent fractionation using sample-

standard bracketing and internal normalization to $^{50}Cr/^{52}Cr$ applying an exponential mass fractionation law and a $^{50}Cr/^{52}Cr$ ratio of 0.051859 (Shields et al., 1966). Chromium isotopic anomalies are reported in ε notation, as defined below:

$$\varepsilon\,^{x}Cr = \left[\frac{\left({}^{x}Cr/{}_{52}Cr\right)_{sample}}{\left({}^{x}Cr/{}_{52}Cr\right)_{standard}} - 1\right] * 10^{4}$$

Where x is mass 53 or 54 and ratios have been internally normalized.

To assess the accuracy and precision of our methodology for Cr isotope analyses (including chemical separation and mass spectrometry), we purified and measured Cr in the Smithsonian Allende reference powder alongside samples. Our external reproducibility (2SD) based on repeat measurements of pure synthetic Cr standards as well as the Allende reference powder in our laboratory is ± 0.07 for $\varepsilon^{53}Cr$ and ± 0.13 for $\varepsilon^{54}Cr$ (See Fig. EA3 in Torrano et al., 2021).

3. RESULTS

3.1 Rare Earth Element (REE) Concentrations

The REE concentrations for a subset of the CAIs included in this study were reported previously (Torrano et al., 2019). Those data, along with the REE concentrations for the CAIs reported here for the first time, are given in Table 2 and shown in Fig. 1. Unfractionated group I REE patterns, interpreted to represent condensation from a gas of solar composition (Martin and Mason, 1974; MacPherson, 2014), are observed in five CAIs. Highly fractionated group II REE patterns, which are interpreted to represent evaporation of preexisting materials followed by near-equilibrium recondensation (Hu et al., 2021), are observed in six CAIs. A slightly fractionated group III REE pattern, interpreted to be associated with multiple heating/cooling events under changing redox conditions (Ruzicka et al., 2012), is observed in one CAI. In the sample set studied here, all fine-grained CAIs exhibit fractionated REE patterns while coarse-grained CAIs generally exhibit unfractionated REE patterns (Table 1).

Table 2. REE concentrations in the CAIs studied here (concentrations in ppm, uncertainties are ± 5%, 2SD).

Sample	La	Ce	Pr	Nd	Sm	Eu	Gd	Tb	Dy	Ho	Er	Tm	Yb	Lu
ZT1[1]	4.86	12.24	1.72	9.25	3.10	1.16	3.80	0.75	5.57	1.46	4.81	0.57	3.66	0.72
ZT2[1]	4.53	12.59	1.87	10.26	3.51	0.77	1.94	0.32	1.68	0.18	0.42	0.51	1.93	0.06
ZT3[1]	1.38	11.08	1.02	4.20	2.32	0.36	0.34	0.06	0.33	0.03	0.04	0.42	0.80	0.01
ZT5[1]	0.24	1.83	0.11	0.58	0.16	0.85	0.11	0.02	0.13	0.02	0.05	0.05	0.96	0.00
ZT6	2.63	7.38	1.05	5.70	2.15	0.82	2.92	0.54	3.87	0.97	3.25	0.37	2.53	0.41
ZT7[1]	3.64	9.06	1.41	7.78	2.73	1.30	3.16	0.59	4.22	0.91	2.71	0.45	2.38	0.40
ZT8[1]	4.52	11.89	1.66	9.14	2.97	0.75	3.59	0.69	5.07	1.06	3.35	0.49	2.29	0.49
ZT10	0.68	3.34	0.39	1.73	0.90	0.17	0.24	0.04	0.23	0.01	0.03	0.16	0.35	0.00
ZT13	1.48	8.02	0.87	3.80	1.87	0.20	0.28	0.05	0.29	0.03	0.08	0.26	0.68	0.01
ZT14	5.41	13.88	2.00	10.64	3.76	1.30	4.94	0.90	6.45	1.41	4.32	0.63	4.28	0.65
Saguaro	0.78	1.82	0.29	1.61	0.51	0.27	0.87	0.15	0.99	0.19	0.55	0.08	0.54	0.07

[1]Data from Torrano et al. (2019).

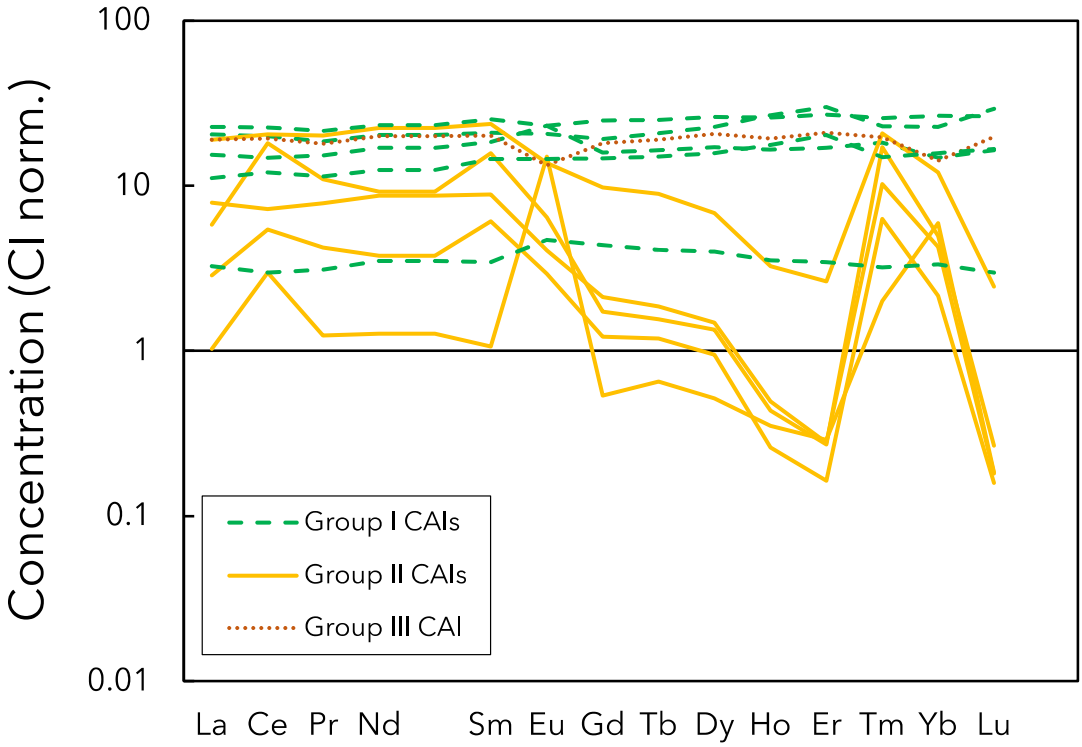

Fig. 1. The REE abundances in the CAIs studied here normalized to REE abundances in CI chondrites (Lodders, 2003). Uncertainties are ± 5%, 2SD.

3.2 Titanium and Chromium Isotopic Compositions

The mass-independent Ti and Cr isotopic compositions of the CAIs studied here are shown in Table 3 and Fig. 2. Also shown in Table 3 are the Ti and Cr isotopic compositions of the terrestrial rock standards BCR-2 and AGV-1 and the Smithsonian Allende reference powder. We note that our data for the terrestrial rock standards BCR-2 and AGV-1 do not show any Ti isotope

anomalies within uncertainties and our data for the Allende reference powder are consistent with previously reported Ti (Zhang et al., 2011, 2012; Sanborn et al., 2019) and Cr (Shukolyukov and Lugmair, 2006; Trinquier et al., 2007; Qin et al., 2010; Williams et al., 2020; Zhu et al., 2021) isotopic compositions for this chondrite. These results demonstrate the accuracy of our chemical processing and mass spectrometry methods for Cr and Ti isotopic analyses. In the CAIs studied here, ε^{46}Ti values range from 0.89 ± 0.17 to 1.82 ± 0.17, ε^{48}Ti values range from 0.04 ± 0.07 to 0.55 ± 0.07, and ε^{50}Ti values range from 8.88 ± 0.17 to 10.68 ± 0.17. For Cr, ε^{53}Cr values range from –1.46 ± 0.14 to –0.34 ± 0.07 and ε^{54}Cr values range from +3.16 ± 0.13 to 7.28 ± 0.16. All measured ε^{53}Cr values (hereafter $\varepsilon^{53}Cr_m$) have been corrected (reported hereafter as $\varepsilon^{53}Cr_c$) for the presence of radiogenic ^{53}Cr from the decay of ^{53}Mn by subtracting an estimated radiogenic ^{53}Cr component assuming an initial Solar System $^{53}Mn/^{55}Mn$ ratio of $7 \pm 1 \times 10^{-6}$ (Tissot et al., 2017) and the $^{55}Mn/^{52}Cr$ measured in these samples; the uncertainty associated with this correction calculation has been incorporated into the reported uncertainty.

Table 3. Titanium and Cr isotopic compositions of the non-Allende CAIs studied here, as well as the BCR-2 and AGV-1 terrestrial rock standards and the Smithsonian Allende reference powder. Also listed are the measured $^{55}Mn/^{52}Cr$ for each CAI (errors on these ratios are estimated to be ±5%). The reported error for the isotope values is either the internal error (2SE) based on the number of repeat runs (n) of each sample or the external reproducibility (2SD), whichever is larger. The uncertainty associated with the correction for the radiogenic component has been incorporated into the reported error for $\varepsilon^{53}Cr_c$. For the terrestrial rock standards and Allende, each entry in a separate row represents a separately processed aliquot.

Sample	$\varepsilon^{46}Ti$	$\varepsilon^{48}Ti$	$\varepsilon^{50}Ti$	n (Ti)	$\varepsilon^{53}Cr_c$[2]	$\varepsilon^{54}Cr$	n (Cr)	$^{55}Mn/^{52}Cr$
ZT1[1]	1.21 ± 0.35	0.36 ± 0.07	9.50 ± 0.17	2	–1.46 ± 0.14	6.05 ± 0.13	6	0.635
ZT2[1]	1.63 ± 0.17	0.46 ± 0.09	9.07 ± 0.17	3	–1.18 ± 0.07	6.99 ± 0.16	3	0.107
ZT3[1]	1.69 ± 0.17	0.38 ± 0.07	10.68 ± 0.17	3	–0.62 ± 0.07	3.16 ± 0.13	7	0.114
ZT5[1]	1.40 ± 0.39	0.34 ± 0.07	9.04 ± 0.17	2	–0.65 ± 0.07	5.32 ± 0.15	3	0.226
ZT6	1.51 ± 0.17	0.55 ± 0.07	8.95 ± 0.20	4	–1.11 ± 0.12	5.37 ± 0.16	5	1.677
ZT7[1]	1.53 ± 0.17	0.40 ± 0.07	8.88 ± 0.17	3	–0.34 ± 0.07	3.41 ± 0.29	1	0.443
ZT8[1]	1.56 ± 0.17	0.43 ± 0.07	9.18 ± 0.17	3	–1.26 ± 0.07	7.28 ± 0.16	3	0.166
ZT10	0.89 ± 0.17	0.04 ± 0.07	10.45 ± 0.17	4	–0.63 ± 0.07	3.50 ± 0.13	5	0.159
ZT13	1.63 ± 0.26	0.41 ± 0.07	9.87 ± 0.27	5	–0.97 ± 0.07	5.66 ± 0.25	3	1.603
ZT14	1.74 ± 0.28	0.30 ± 0.07	9.16 ± 0.19	4	–0.64 ± 0.07	4.90 ± 0.13	5	0.460
Saguaro	1.82 ± 0.17	0.47 ± 0.10	9.38 ± 0.35	4	–1.12 ± 0.07	6.15 ± 0.31	4	1.291
AGV-1[1]	–0.14 ± 0.23	0.00 ± 0.07	0.08 ± 0.21	5				
AGV-1[1]	–0.07 ± 0.21	0.08 ± 0.09	–0.04 ± 0.17	5				
BCR-2[1]	–0.01 ± 0.17	–0.02 ± 0.08	–0.04 ± 0.17	8				
BCR-2[1]	–0.10 ± 0.17	0.01 ± 0.07	–0.09 ± 0.17	20				
BCR-2	–0.02 ± 0.34	0.09 ± 0.11	–0.15 ± 0.22	4				
Allende[1]	0.47 ± 0.34	–0.08 ± 0.23	3.08 ± 0.17	3				
Allende[1]	0.60 ± 0.17	0.00 ± 0.07	3.30 ± 0.17	32				
Allende	0.46 ± 0.17	0.01 ± 0.07	3.04 ± 0.21	4				
Allende					–0.21 ± 0.07	0.81 ± 0.13	10	
Allende					–0.25 ± 0.07	0.88 ± 0.13	6	

[1]Ti isotopic data from Torrano et al. (2019).
[2]All $\varepsilon^{53}Cr_c$ data are corrected for the decay of ^{53}Mn (see text for details).

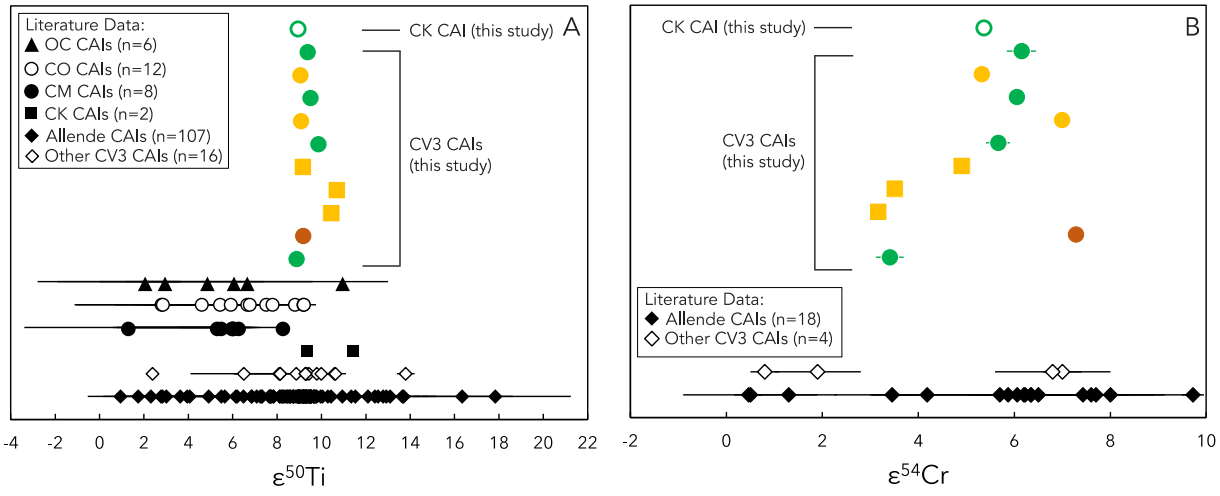

Fig. 2. The (A) $\varepsilon^{50}Ti$ and (B) $\varepsilon^{54}Cr$ values for the CAIs analyzed here (colored symbols); the different colors and symbols correspond to the REE patterns and textures for these CAIs (see the legend and caption in Fig. 3). For comparison, literature data are shown for CAIs from the Allende

CV3 chondrite (solid black diamonds; Heydegger et al., 1979; Niederer et al., 1980, 1981, 1985; Niemeyer and Lugmair, 1981, 1984; Birck and Allègre, 1984, 1985; Papanastassiou, 1986; Birck and Lugmair, 1988; Trinquier et al., 2007, 2009; Chen et al., 2009; Leya et al., 2009; Williams et al., 2016; Davis et al., 2018; Burkhardt et al., 2019; Torrano et al., 2019; Shollenberger et al., 2022), other CV3 chondrites (open black diamonds; Niederer et al., 1981, 1985; Loss et al., 1994; Leya et al., 2009; Trinquier et al., 2009; Larsen et al., 2011; Simon et al., 2017; Torrano et al., 2019; Shollenberger et al., 2022), CK chondrites (solid black squares; Torrano et al., 2019), CM chondrites (solid black circles; Render et al., 2019), CO chondrites (open black circles; Ebert et al., 2018; Render et al., 2019), and ordinary chondrites (solid black triangles; Ebert et al., 2018).

4. DISCUSSION

4.1 Ruling out matrix addition effects on Cr isotopic compositions of CAIs

The CAIs studied here exhibit greater variability in ε^{54}Cr values compared to ε^{50}Ti values (Fig. 2). The significantly higher Cr concentration and lower ε^{54}Cr of the carbonaceous chondrite matrix (Schneider et al. 2020) compared to CAIs means that a small addition of matrix to a CAI (possibly during parent body or terrestrial alteration or in the laboratory during sample extraction), could have a substantial effect on the measured Cr isotopic composition. In contrast, ε^{50}Ti is less susceptible to matrix addition effects because of the significantly higher Ti concentration in CAIs compared to the carbonaceous chondrite matrix (Gerber et al. 2017). By using the bulk CI chondrite composition as an approximation of the carbonaceous chondrite matrix composition, we use a two-component mixing model (illustrated in Fig. 3) to show that if the maximum ε^{54}Cr value measured in these CAIs is assumed to be the matrix-free CAI value, the entire range in ε^{54}Cr values for the CAIs measured here could be accounted for by the addition of 0–30% CI-like matrix material to the CAIs. The matrix endmember shown in Fig. 3 is defined by the elemental abundances (Alexander et al., 2019) and average of the Ti and Cr isotopic compositions (Shukolyukov and Lugmair, 2006; Trinquier et al., 2007, 2009; Qin et al., 2010; Larsen et al., 2011; Zhang et al., 2012; Schiller et al., 2014; Williams et al., 2020; Zhu et al., 2021) previously reported for CI chondrites. The CAI endmember of the mixing line A (CAI endmember "A" shown as the solid black diamond in Fig. 3) is defined by the mean elemental abundances in the CAIs studied here and in Torrano et al. (2019), the median value of ε^{50}Ti = 9 for CAIs studied here and in the literature, and the maximum value of ε^{54}Cr (= 7.28 ± 0.16) for CAIs studied here. Because of the isotopic variability observed in ε^{50}Ti, we have also plotted mixing line B in Fig. 3 that is similar to mixing line A except for the ε^{50}Ti value for the CAI endmember, which in this case is the maximum value of ε^{50}Ti (= 10.68 ± 0.17) for the CAIs studied here (which is somewhat higher

than the median value and defines CAI endmember "B" shown as the open black diamond in Fig. 3). Figure 3 illustrates that the measured ε^{50}Ti and ε^{54}Cr values in CAIs could fall along such mixing lines with the CI chondrite matrix if most normal CAIs were originally characterized by only a small range in ε^{50}Ti (~9-11) and similar ε^{54}Cr values (~7).

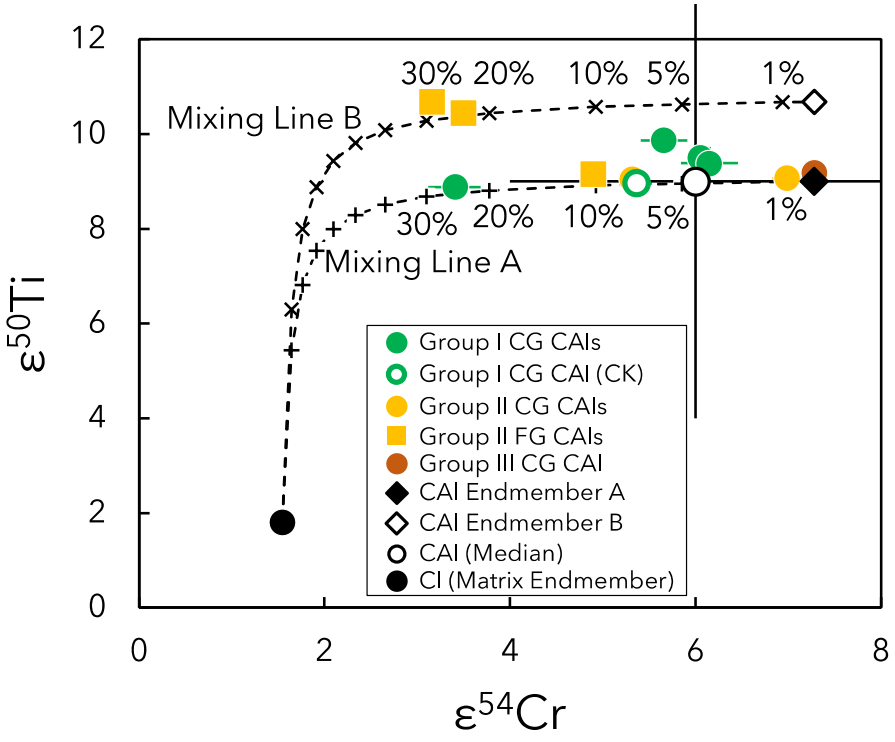

Fig. 3. Mixing lines between the bulk CI chondrite composition (solid black circle, assumed to represent the matrix endmember composition) and (1) a CAI endmember "A" composition represented by the median ε^{50}Ti value for all CAIs and the maximum ε^{54}Cr value for CAIs studied here (solid black diamond; mixing line A denoted by + symbols), and (2) a CAI endmember "B" composition represented by the maximum ε^{50}Ti value for the CAIs studied here and the maximum ε^{54}Cr value for CAIs studied here (open black diamond; mixing line B denoted by × symbols). The two mixing lines are annotated with the percentage of matrix added to the two endmember CAI compositions. The CI chondrite isotopic data are from the literature (Shukolyukov and Lugmair, 2006; Trinquier et al., 2007; Qin et al., 2010; Larsen et al., 2011; Zhang et al., 2012; Schiller et al., 2014; Williams et al., 2020; Zhu et al., 2021). The CI chondrite elemental composition is from Alexander et al. (2019) and references therein, and the elemental concentrations for CAIs are the mean concentrations in the CAIs studied here and in Torrano et al. (2019). The open black circle represents the median ε^{50}Ti and ε^{54}Cr values for all CAIs studied here and in the literature, with 2SD error bars (from the data shown in Fig. 2). The colored symbols show the data for the CAIs studied here (solid symbols are the 11 CV3 CAIs; open symbol is the CK CAI).

Although Fig. 3 demonstrates that the addition of ~0–30% matrix material to CAIs could account for the small range in ε^{50}Ti and more significant variability in ε^{54}Cr values measured here, additional data must be examined to determine whether matrix addition is in fact responsible. If matrix addition was the main cause of the variability in ε^{54}Cr values, these values should be linearly correlated with the inverse of the Cr concentration. Figure 4 demonstrates that such a correlation is not apparent. This also argues against varying degrees of secondary alteration as a cause of the observed ε^{54}Cr variability. Although the lowest ε^{54}Cr value is measured in a fine-grained CAI with a high Cr concentration (ZT3), similarly low ε^{54}Cr values are also reported for CAIs with lower Cr concentrations. This suggests that while matrix addition may at least partially account for the low ε^{54}Cr composition of ZT3, it cannot account for the full range of ε^{54}Cr values measured in the CAIs in this sample set. Furthermore, great care was taken during sample extraction to avoid matrix contamination, and although a range of ~0–30% matrix addition would be easily visible in the samples, no matrix addition was observed. Previously published ε^{54}Cr values for CAIs span a range of ~0 to ~10, including a handful of samples with ε^{54}Cr values that are below the ε^{54}Cr value of CI chondrites (Birck and Allègre, 1984; Birck and Lugmair, 1988; Loss et al., 1994). Such values cannot be accounted for by matrix addition and therefore indicate that the variability in ε^{54}Cr observed in CAIs is inherent to the CAIs themselves. A more likely explanation for the greater variability in ε^{54}Cr compared to ε^{50}Ti is the variable distribution of the carrier phases of these anomalies, and these data could be interpreted as additional evidence that these isotopes have distinct carrier phases. It is also possible that thermal processing in the disk affected these distinct carrier phases differently and this contributed to the differences in their variability in CAIs.

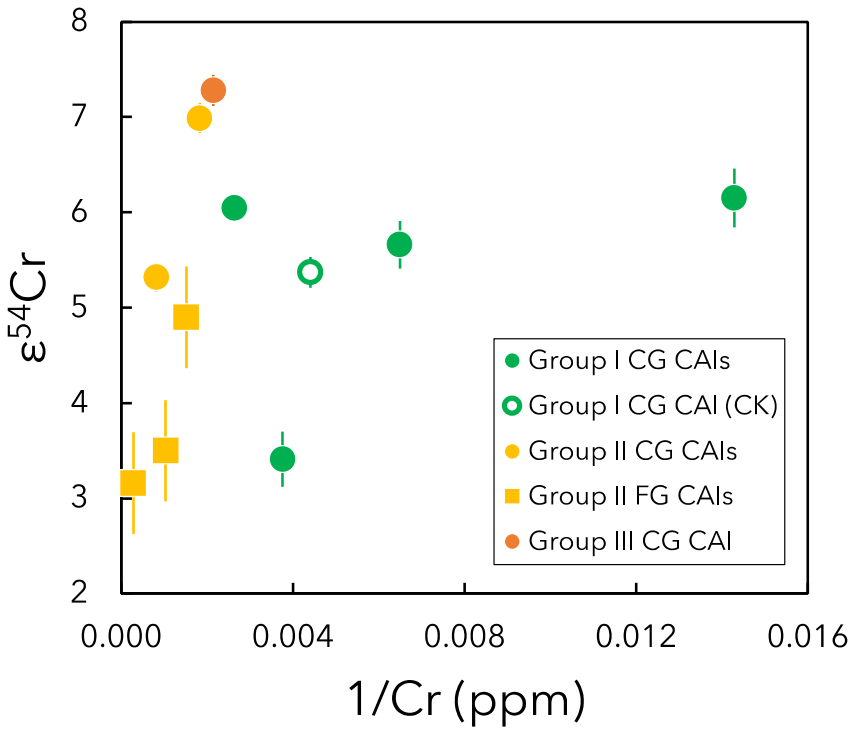

Fig. 4. The ε^{54}Cr values versus 1/Cr (ppm) concentrations for the CAIs studied here. In general, the highest Cr concentrations are measured in the fine-grained CAIs (squares) and those with Group II REE patterns (yellow symbols), suggesting that fine-grained CAIs are more susceptible to matrix addition and/or that matrix addition may be more difficult to identify in these samples via optical microscope and electron microprobe analyses because of their fine-grained mineralogy.

4.2 The relationship between REE patterns and isotopic anomalies

Fractionated REE patterns in CAIs are considered to originate because of differences in thermal conditions and processing in the CAI-forming region of the nebula. If these conditions were the same as those responsible for selective destruction of isotopically distinct presolar phases (as suggested by Trinquier et al., 2009), one would expect to observe a correlation between the degree of fractionation in the REEs and the isotopic anomalies in CAIs. To assess whether such a correlation exists, we plot both ε^{50}Ti and ε^{54}Cr versus chondrite-normalized La/Lu (i.e., $[La/Lu]_{CI}$) for CAIs in this study (Fig. 5). While the highest ε^{50}Ti values are reported in fine-grained CAIs with fractionated REE patterns (i.e., $[La/Lu]_{CI} >> 1$), these CAIs do not have the highest ε^{54}Cr values. In neither case is there a clear correlation between isotopic compositions and the degree of fractionation of the REE patterns in CAIs, which is consistent the results of Davis et al. (2018).

This lack of correlation suggests that the processes leading to the isotopic anomalies observed in CAIs were distinct from the conditions responsible for the observed REE patterns.

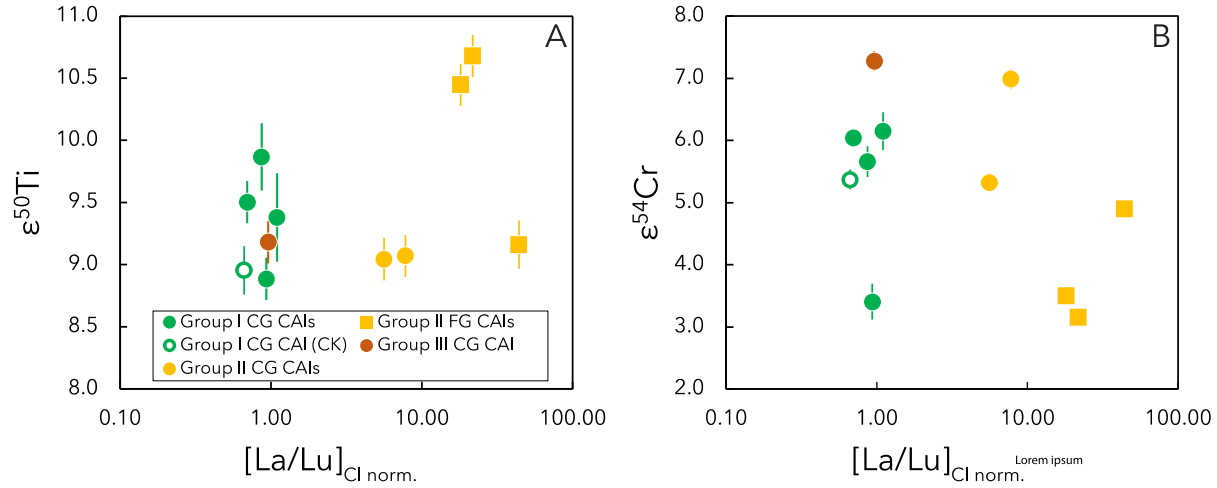

Fig. 5. The ε^{50}Ti (A) and ε^{54}Cr (B) values for the CAIs analyzed here plotted versus their chondrite-normalized La/Lu (i.e., [La/Lu]/CI); chondritic abundances are from Lodders (2003).

4.3 CAI isotopic compositions record the averaging of isotopically anomalous precursors

The CAIs studied here show resolvable variability in both ε^{54}Cr and ε^{50}Ti that likely reflects isotopic variability in the protoplanetary disk recorded during CAI formation. This could result from isotopic variability in the CAI precursor materials, variable distribution of the carrier phases of isotopic anomalies, and/or differences in the thermal processing experienced by CAIs and their precursors in the disk. It has been proposed previously that different thermal processing histories in the disk could cause different degrees of volatilization of isotopically anomalous carriers that were initially homogeneously distributed and could thereby create isotopic heterogeneity (e.g., Trinquier et al, 2009). It is important to consider, however, that the carrier phase of Cr (a moderately refractory element) appears to be refractory sub-micron spinel grains (Dauphas et al., 2010, Qin et al., 2011), which complicates any broad interpretation of the effect of thermal processing on the isotope compositions of refractory vs. moderately refractory elements in the disk and emphasizes the need for the identification and characterization of the carrier phases of isotopic anomalies. It is unlikely that thermal processing in the disk can fully account for the observed Ti and Cr isotopic anomalies in CAIs, although it may account for some of the observed variability. It is likely that the isotopic variability in CAIs reflects variability in the distribution, as

well as the degree of mixing and averaging of isotopically anomalous CAI precursor materials (including the carrier phases of these isotopic anomalies).

The isotopic compositions of CAIs define a relatively narrow range when compared to other early-formed refractory solids such as PLACs and SHIBs, or presolar grains. PLACs have low inferred initial $^{26}Al/^{27}Al$ and large isotopic anomalies and are thought to have formed prior to CAIs (Fahey et al., 1987; Ireland, 1988; Ireland et al., 1990; Liu et al., 2009; Kööp et al., 2016a). SHIBs have variable inferred $^{26}Al/^{27}Al$ values that are consistent with the canonical value within analytical uncertainty, a more restricted range of isotopic anomalies, and are suggested to have formed after PLACs but prior to CAIs (Fahey et al., 1987; Ireland, 1988; Ireland et al., 1990; Kööp et al., 2016b; Liu et al., 2019). The FUN CAIs have larger isotopic anomalies than CAIs (but smaller than PLACs); their low inferred $^{26}Al/^{27}Al$ combined with their high degree of mass-dependent fractionation could indicate their formation either before or after normal CAIs (MacPherson, 2014). In the case of $\varepsilon^{50}Ti$, normal CAIs exhibit a narrow range and significant peak near the median value (range ~0 to ~16, median = ~9; Heydegger et al., 1979; Niederer et al., 1980, 1981, 1985; Niemeyer and Lugmair, 1981, 1984; Loss et al., 1994; Chen et al., 2009; Leya et al., 2009; Trinquier et al., 2009; Williams et al., 2016; Simon et al., 2017; Davis et al., 2018; Ebert et al., 2018; Burkhardt et al., 2019; Render et al., 2019; Torrano et al., 2019; Shollenberger et al., 2022), while PLACs (range ~ –700 to ~2500, median ~50; Ireland et al., 1990; Sahijpal et al., 2000; Liu et al., 2009; Kööp et al., 2016a) and SHIBs (range ~ –60 to ~150, median ~ 20; Ireland et al., 1990; Sahijpal et al., 2000; Liu et al., 2009; Kööp et al., 2016b) have wider ranges but similar peaks near their median values (Fig. 6). The wider range of $\varepsilon^{50}Ti$ values in the PLACs and SHIBs compared to the likely somewhat later-formed CAIs has been interpreted to record multiple generations of refractory materials present in the early Solar System that progressed from the highly isotopically anomalous ones (like PLACs) to somewhat less isotopically anomalous (like SHIBs) to minimally isotopically anomalous (like the normal CAIs), all before the accretion of parent bodies of bulk meteorites (e.g., Kööp et al., 2016a; Render et al., 2019; Torrano et al., 2019). The combination of a progressively smaller isotopic range of $\varepsilon^{50}Ti$ values from PLACs to SHIBs to CAIs and the similar median $\varepsilon^{50}Ti$ values for each of these populations further suggests that the $\varepsilon^{50}Ti$ compositions of CAIs likely record a progressive degree of mixing and homogenization of the more isotopically anomalous PLACs and SHIBs and the resulting averaging of their isotopic anomalies.

The small size of PLACs and SHIBs (~50 μm) compared to CAIs (up to cm-scale) suggests that CAIs could incorporate enough of these smaller precursors to account for the smaller range in the CAI isotopic compositions. Recent work by Shollenberger et al. (2022) quantified this observation using the central limit theorem and demonstrated that the Ti isotopic compositions (including ε^{46}Ti, ε^{48}Ti, ε^{50}Ti) of CAIs can be explained by the averaging of hibonite inclusions. This trend also extends to presolar grains, which exhibit an ε^{50}Ti range of ~ –5000 to ~5000 and a median value of ~400, although the uncertainties on these isotopic measurements are very large (Fig. 6; Ireland et al., 1991; Hoppe et al., 1994; Alexander and Nittler, 1999; Amari et al., 2001a, b; Huss and Smith, 2007; Zinner et al., 2007; Gyngard et al., 2018). Presolar grains may be initial carriers of the ^{50}Ti anomalies incorporated into the most isotopically anomalous early-formed refractory solids such as PLACs, and an averaging effect could explain the progression of decreasing ranges in the sizes of the isotopic anomalies from presolar grains to PLACs, then to SHIBs, and then to CAIs. Measurements of large ^{54}Cr anomalies (ε^{54}Cr > 25,000) in presolar grains suggest that these are also the initial carriers of the ^{54}Cr anomalies (e.g., Dauphas et al., 2010; Qin et al., 2011; Nittler et al., 2018).

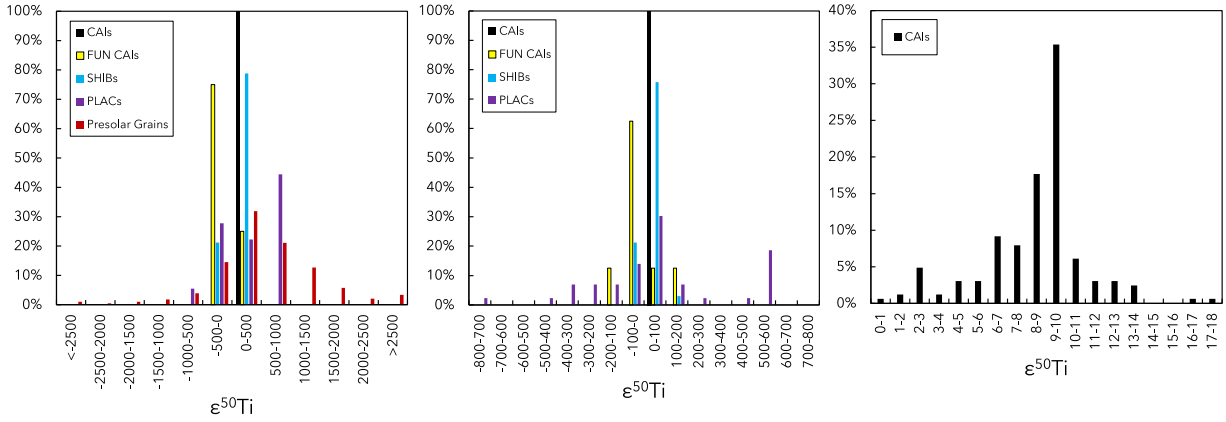

Fig. 6. Histograms of ε^{50}Ti values reported for CAIs (n = 162; Heydegger et al., 1979; Niederer et al., 1980, 1981, 1985; Niemeyer and Lugmair, 1981, 1984; Birck and Allègre, 1984, 1985; Papanastassiou, 1986; Birck and Lugmair, 1988; Loss et al., 1994; Chen et al., 2009; Leya et al., 2009; Larsen et al., 2011; Trinquier et al., 2009; Williams et al., 2016; Simon et al., 2017; Davis et al., 2018; Ebert et al., 2018; Burkhardt et al., 2019; Render et al., 2019; Torrano et al., 2019; Shollenberger et al., 2022), FUN CAIs (n = 8; Niederer et al., 1981; Fahey et al., 1987; Papanastassiou and Brigham, 1989; Loss et al., 1994; Williams et al., 2016), SHIBs (n = 33; Ireland, 1990; Sahijpal et al., 2000; Liu et al., 2009; Kööp et al., 2016b), PLACs (n = 43; Ireland, 1990; Sahijpal et al., 2000; Liu et al., 2009; Kööp et al., 2016a), and presolar grains (n = 379; Ireland et al., 1991; Hoppe et al., 1994; Alexander and Nittler, 1999; Amari et al., 2001a, b; Huss

and Smith, 2007; Zinner et al., 2007; Gyngard et al., 2018). FUN CAIs are plotted with CAIs in the two panels on the left, but not in the right-most panel.

A possible extension of the averaging effect observed in the isotopic anomalies in PLACs and SHIBs compared to CAIs is seen within the CAI population studied here, where a wider variation in both ε^{50}Ti and ε^{54}Cr is observed in CAIs of smaller extracted mass and the ε^{50}Ti and ε^{54}Cr compositions converge toward the median ε^{50}Ti and ε^{54}Cr values with increasing CAI extracted mass (Fig. 7). This trend should be viewed with caution because there is an inexact correlation between the extracted mass and the mass of the whole CAI. For instance, a CAI exposed in 2D in a meteorite slab (and extracted from it) does not represent its full size and mass. Nevertheless, in most cases we may assume that the mass of each CAI that was extracted and dissolved in this study (and in Torrano et al., 2019) generally correlates with its size. This apparent convergence towards the median isotopic composition seen in Fig. 7 could provide additional evidence for the averaging effect on isotopic anomalies from smaller to larger inclusions. A correlation between the magnitude of ^{54}Cr anomalies and grain size is also reported in separates of nanospinels from Orgueil (Dauphas et al., 2010) and in presolar grains (Nittler et al., 2018). Therefore, the apparent presence of such a correlation in both presolar grains and CAIs may indeed record the averaging effect of mixing and homogenization of progressively larger solids through time and the continuous averaging and dilution of isotopic anomalies from the presolar grains that contributed to the initial mass of materials from which the solar nebula formed, through the formation of CAIs in the early Solar System.

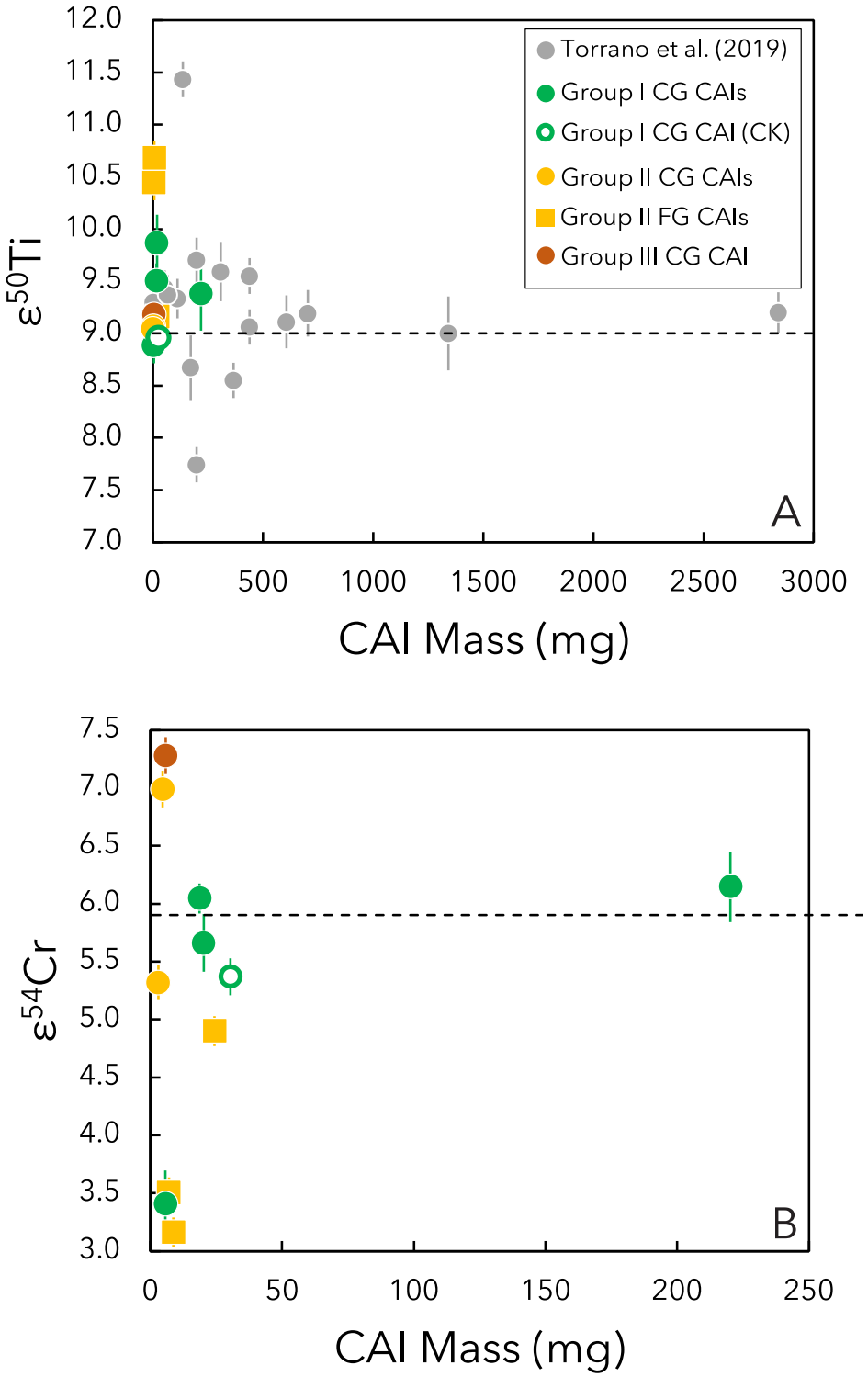

493

494 Fig. 7. A) ε^{50}Ti vs. the extracted mass of the CAIs studied here (colored symbols) and from Torrano
495 et al. (2019) (solid gray circles), and B) ε^{54}Cr vs. the extracted mass of the CAIs studied here
496 (colored symbols). Dashed lines denote the median ε^{50}Ti and ε^{54}Cr values for all CAIs studied
497 here and from the literature (Heydegger et al., 1979; Niederer et al., 1980, 1981, 1985; Niemeyer

and Lugmair, 1981, 1984; Birck and Allègre, 1984, 1985; Papanastassiou, 1986; Birck and Lugmair, 1988; Loss et al., 1994; Chen et al., 2009; Leya et al., 2009; Trinquier et al., 2009; Larsen et al., 2011; Williams et al., 2016; Davis et al., 2018; Ebert et al., 2018; Render et al., 2019; Burkhardt et al., 2019; Torrano et al., 2019; Shollenberger et al., 2022).

4.4 Identifying the nucleosynthetic sources of Ti and Cr isotopic anomalies

The CAIs studied here and previously together exhibit a correlation between ε^{46}Ti and ε^{50}Ti that corresponds to a slope of 5.63 ± 0.29 and an intercept of 0.19 ± 0.45 (indistinguishable considering errors to the slope and intercept based on the CAI data of Torrano et al., 2019, and references therein, shown as the dashed black line in Fig. 8A), and NC and CC bulk meteorites fall close to this CAI correlation line (Fig. 8A). As discussed by Torrano et al. (2019), this correlation likely represents the mixing between a ^{46}Ti- and ^{50}Ti-poor reservoir and a ^{46}Ti- and ^{50}Ti-rich reservoir. The isotopes ^{46}Ti and ^{50}Ti are produced by distinct nucleosynthetic sources, with ^{46}Ti produced during explosive oxygen- and silicon-burning at the top of the Si/S zone in Type II supernovae (SNII) and ^{50}Ti potentially produced in multiple sources, including Type Ia supernovae (SNIa), the O/Ne and O/C zones of SNII (while it is destroyed in the explosive burning zones where other Ti isotopes are produced), and electron-capture supernovae (ECSN) (Rauscher et al., 2002; Woosley et al., 2002; Wanajo et al., 2013; Davis et al., 2018; Nittler et al., 2018). As such, the reservoir enriched in both ^{46}Ti and ^{50}Ti isotopes must itself have resulted from the mixing of materials from two distinct reservoirs (one enriched in ^{46}Ti and the other enriched in ^{50}Ti). Therefore, this correlation suggests the presence of materials from at least three distinct isotopic reservoirs during Solar System formation. This correlation does not extend to all PLACs and SHIBs (Fig. 8B), but the PLACs and SHIBs with smaller isotopic anomalies generally do plot (within the errors) on the CAI correlation line (Fig. 8C). This provides further evidence that the averaging of the isotopic compositions of these objects may be responsible for the isotopic compositions of the CAIs.

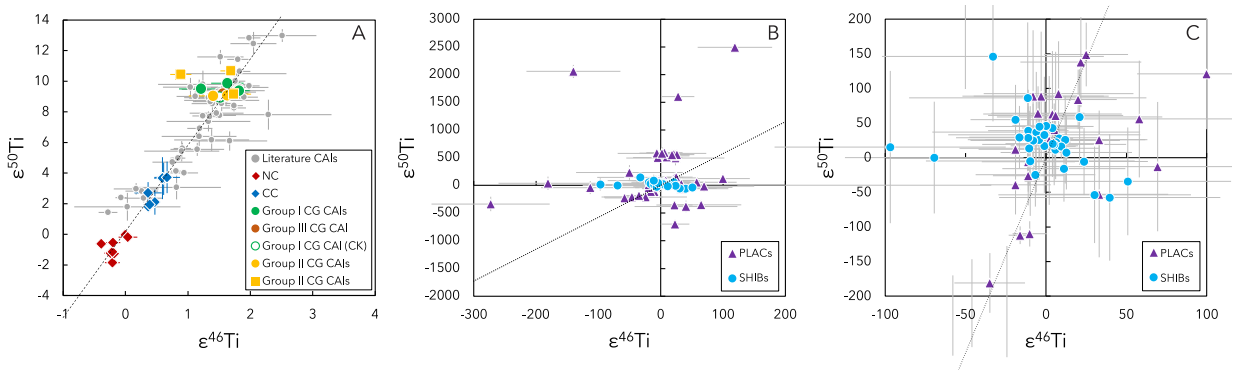

526

527 Fig. 8. (A) ε^{50}Ti vs. ε^{46}Ti for the CAIs analyzed here (colored circles) and from the literature (solid
528 gray circles) (Leya et al., 2009; Trinquier et al., 2009; Davis et al., 2018; Ebert et al., 2018;
529 Burkhardt et al., 2019; Render et al., 2019; Torrano et al., 2019; Shollenberger et al., 2022), and
530 for bulk NC and CC samples (Trinquier et al., 2009; Zhang et al., 2011, 2012; Sanborn et al., 2019;
531 Williams et al., 2020; Torrano et al., 2021). (B) ε^{50}Ti vs. ε^{46}Ti for PLACs and SHIBs from the
532 literature (Ireland et al., 1990; Sahijpal et al., 2000; Liu et al., 2009; Kööp et al., 2016a, 2016b).
533 (C) Data from panel (B) zoomed in to illustrate that PLACs and SHIBs with smaller isotopic
534 anomalies plot, within the errors, on the CAI correlation line. The black dashed line in all panels
535 is the ε^{50}Ti vs. ε^{46}Ti correlation line for CAIs based on all CAI data shown in panel (A).
536

537 The CAIs studied here appear to exhibit an anti-correlation between $\varepsilon^{53}Cr_c$ and ε^{54}Cr (Fig.
538 9), but it is unclear whether such a trend holds for all CAIs. In this context, it should be noted that
539 the $\varepsilon^{53}Cr_c$ values shown in Fig. 9 for CAIs from this study and bulk meteorites from the literature
540 have been corrected for the decay of ^{53}Mn based on their measured Mn/Cr and assuming an initial
541 $^{53}Mn/^{55}Mn$ ratio of $7\pm1 \times 10^{-6}$ (Tissot et al., 2017). However, the ε^{53}Cr values of CAIs from the
542 literature have not been corrected similarly because Mn/Cr for these samples are not always
543 reported. This, along with the typically larger uncertainties associated with the ε^{53}Cr values of
544 CAIs reported in the literature, may be the reason for the apparent lack of a clear anti-correlation
545 trend in these data in Fig. 9.

546 Overall, the CAIs from this study and the literature exhibit ε^{54}Cr values that are relatively
547 large and positive and ε^{53}Cr and $\varepsilon^{53}Cr_c$ values that are smaller and predominantly somewhat
548 negative (Fig. 9). Presolar grains show significantly larger ^{54}Cr excesses, but limited ^{53}Cr excesses
549 (e.g., Dauphas et al., 2010; Qin et al., 2011; Nittler et al., 2018). These broadly similar isotopic
550 characteristics that are more pronounced in presolar grains and relatively muted in CAIs provide
551 further evidence that supernova-derived presolar grains were likely the original sources of the
552 isotopic anomalies observed in CAIs. Nittler et al. (2018) suggested that, based on the relationship
553 between ^{54}Cr and ^{53}Cr, the primary sources of ^{54}Cr are likely slow-conflagration SNIa that produce

no ^{53}Cr (Woosley, 1997) and fast-deflagration SNIa and ECSN that produce limited ^{53}Cr (Woosley, 1997; Wanajo et al., 2013), and not SNII, which feature ^{54}Cr-rich zones that are also either highly enriched or depleted in ^{53}Cr (Woosley, 1997). These sources of ^{54}Cr-rich grains may also produce ^{50}Ti-rich carrier phases such as perovskite or other oxides.

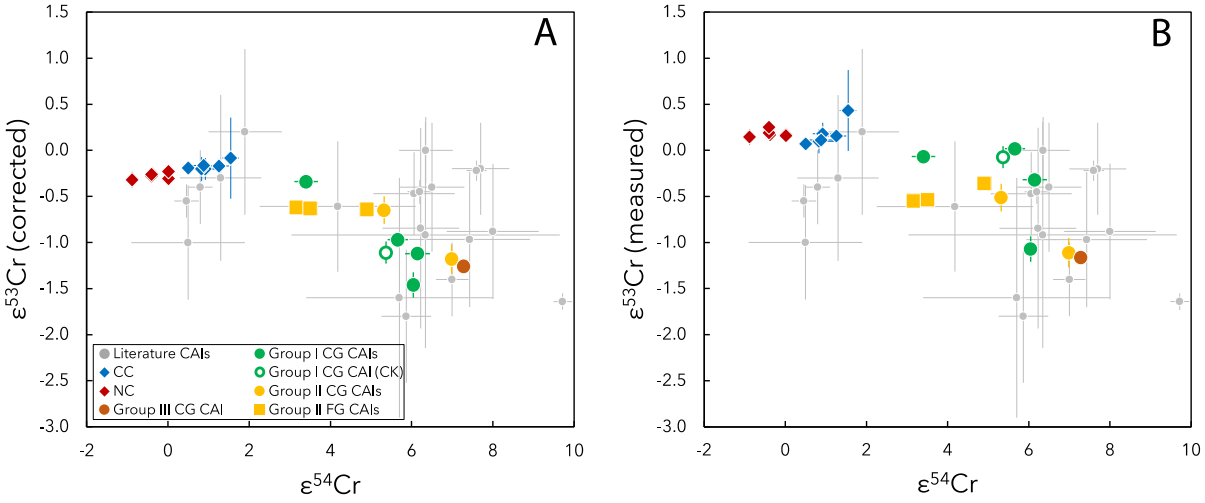

Fig. 9. (A) $\varepsilon^{53}Cr_c$ vs. $\varepsilon^{54}Cr$, and (B) $\varepsilon^{53}Cr_m$ vs. $\varepsilon^{54}Cr$ for the CAIs analyzed here, bulk NC (Trinquier et al., 2007; Qin et al., 2010; Yamakawa et al., 2010; Mougel et al., 2018; Pedersen et al., 2019; Zhu et al., 2021) and CC (Shukolyukov and Lugmair, 2006; Trinquier et al., 2009; Qin et al., 2010; Larsen et al., 2011; Schiller et al., 2014; Göpel et al., 2015; Langbroek et al., 2019; Van Kooten et al., 2020; Williams et al., 2020; Torrano et al., 2021; Zhu et al., 2021) meteorites, and CAIs from the literature (Birck and Allègre, 1984, 1985; Papanastassiou, 1986; Birck and Lugmair, 1988; Loss et al., 1994). Panel A shows $\varepsilon^{53}Cr_c$ (corrected for radiogenic contributions from the decay of ^{53}Mn; see text for details) and panel B shows measured ($\varepsilon^{53}Cr_m$) values. The data for CAIs from the literature are not corrected for ^{53}Mn decay in either panel.

4.5 Clues to the role of CAIs in the origin of the NC–CC isotopic dichotomy

The CC reservoir is enriched relative to the NC reservoir in supernova-derived neutron-rich isotopes, including ^{50}Ti and ^{54}Cr (e.g., Warren, 2011 and references therein), as are most CAIs. The NC meteorites exhibit a strong positive linear correlation in a plot of ε^{50}Ti vs. ε^{54}Cr (red line in Fig. 10), and an extension of this line intersects both the CC and CAI isotopic reservoirs. Because most CC materials contain CAIs and most NC materials do not, this could suggest that the transport of CAIs from the inner (NC reservoir) to the outer (CC reservoir) Solar System accounts for the observed isotopic dichotomy. The isotopic dichotomy is observed in both refractory elements such as Ti and Mo (which are abundant in CAIs) and moderately refractory elements such as Cr and Ni (which are far less abundant in CAIs). Mixing lines between enstatite

chondrites (which fall within the NC group) and the average CAI composition are hyperbolic curves in ε^{50}Ti vs. ε^{54}Cr space that circumvent the CC region (red dashed line in Fig. 10). Therefore, the addition of CAIs *sensu stricto* to material of NC composition cannot account for the Ti and Cr isotopic compositions of the CC reservoir.

The positioning of the CC reservoir along the NC correlation line in the direction of CAIs is consistent with the model of admixture of material characterized by CAI-like isotopic composition but solar chemical abundances to the NC reservoir (e.g., Burkhardt et al., 2019; Nanne et al., 2019; Jacquet et al., 2019; Kruijer et al., 2020). In that model, the isotopic dichotomy formed as the result of temporal changes in the isotopic composition of material inherited by the protoplanetary disk from the molecular cloud during the earliest stages of Solar System formation, followed by lack of mixing of the distinct NC and CC reservoirs during the accretion of meteorite parent bodies. Different stages of isotopically distinct infalling material from the parent molecular cloud could account for the distinct isotopic compositions of the NC and CC reservoirs, with CAIs forming during the early infall stage from material enriched in the supernova-derived neutron-rich isotopes of elements such as Cr, Ni, Ti, and Mo, and recording the isotopic composition of this material before being transported outwards in the disk via radial expansion. This may also explain the similar O isotopic composition of the Sun and CAIs if both formed primarily from the same early infalling material (McKeegan et al., 2011; Kööp et al., 2020). The later infalling material, depleted in supernova-derived neutron-rich isotopes and possessing an NC-like composition, may then have contributed to most of the mass in the inner disk. After infall ceased, mass continued to be accreted by the proto-Sun because of inward transport of material (e.g., Yang and Ciesla, 2012). This inward transport could cause minor mixing to occur between the early infalling material enriched in the neutron-rich isotopes (most of which was transported outwards) and the material in the inner disk depleted in the neutron-rich isotopes. One potential impediment to complete mixing of the inner and outer disk may have been the growth of Jupiter's core, which has been attributed with keeping the NC and CC isotopic reservoirs separated for a period of ~1–4 million years after CAI formation (Kruijer et al., 2017). The resulting final isotopic composition of the CC reservoir in this model is intermediate between that of the earliest infalling material (the isotopic composition recorded by CAIs) and later infalling material (the isotopic composition recorded by the NC reservoir), although the elemental compositions of the earliest and later infalling materials would remain broadly CI-like (i.e., solar).

Trinquier et al. (2009) interpreted the linear regression through NC meteorites, the CI chondrite endmember of the CC reservoir, and CAIs in ε^{50}Ti vs. ε^{54}Cr space to represent thermal processing of precursor material with an initially CI chondrite composition and attributed the CC meteorite isotopic compositional field to the addition of CAIs to a CAI-free matrix similar to CI chondrite composition causing the CC bulk isotopic compositions to plot at various points above the NC–CI–CAI regression line. Bryson and Brennecka (2021) suggested that the CC meteorite bulk isotopic compositions reflect mixing between NC, CI, and CAI compositions, and that different degrees of mixing between NC and CI compositions produce compositions along the solid purple line in Fig. 10; thereafter, the admixing of CAIs (for example, the curved purple dashed line in Fig. 10) could account for the compositions of the CC meteorites that fall above the mixing line between NC meteorites and CI chondrites (solid purple line). However, Williams et al. (2020) demonstrated that when an updated regression line through the NC meteorite data is plotted (solid red line in Fig. 10), it passes through the middle of the CC isotopic reservoir, well above the CI endmember composition (Fig. 10). Therefore, the addition of CAIs to compositions along the NC trendline or an NC–CI–CAI regression line cannot account for the entire range of isotopic compositions of CC meteorites. Instead, the CC meteorites that plot below the NC correlation trend require the addition of materials that are characterized by similar Ti and Cr isotopic compositions to CAIs but lower Ti/Cr or a component enriched in ^{54}Cr such as Cr-rich spinel grains (Williams et al., 2020). This component may be AOAs, which are abundant in carbonaceous chondrites and are considered to have formed from the same isotopic reservoir as CAIs based on oxygen, Cr, and Ti isotopic compositions (e.g., Krot et al., 2004; Trinquier et al., 2009; Larsen et al., 2011). The Ti/Cr of AOAs are reported to be generally much lower than CAIs (Sugiura et al., 2009) resulting in mixing lines between AOA and OC compositions in ε^{50}Ti vs. ε^{54}Cr space to have a shallower (or even opposite) shaped curves compared to the CAI mixing lines (for example, the gray dashed line in Fig. 10 modeled after Williams et al., 2020) and could, therefore, pass through the CC meteorite compositions that fall below the NC regression line. The ^{54}Cr-enriched spinel grains identified in carbonaceous chondrites (Dauphas et al., 2010) contain little Ti, implying that the addition of such materials could also drive isotopic compositions in the horizontal direction below the NC regression line in Fig. 10. As such, the addition of CAIs or material with CAI-like isotopic and elemental compositions to material plotting along the NC regression trend cannot entirely account for the range of compositions in the CC reservoir, the gap

between the NC and CC reservoirs, or the orthogonal trends defined by the meteorites within the NC and CC groups; other chondritic components must play a role in defining these characteristics.

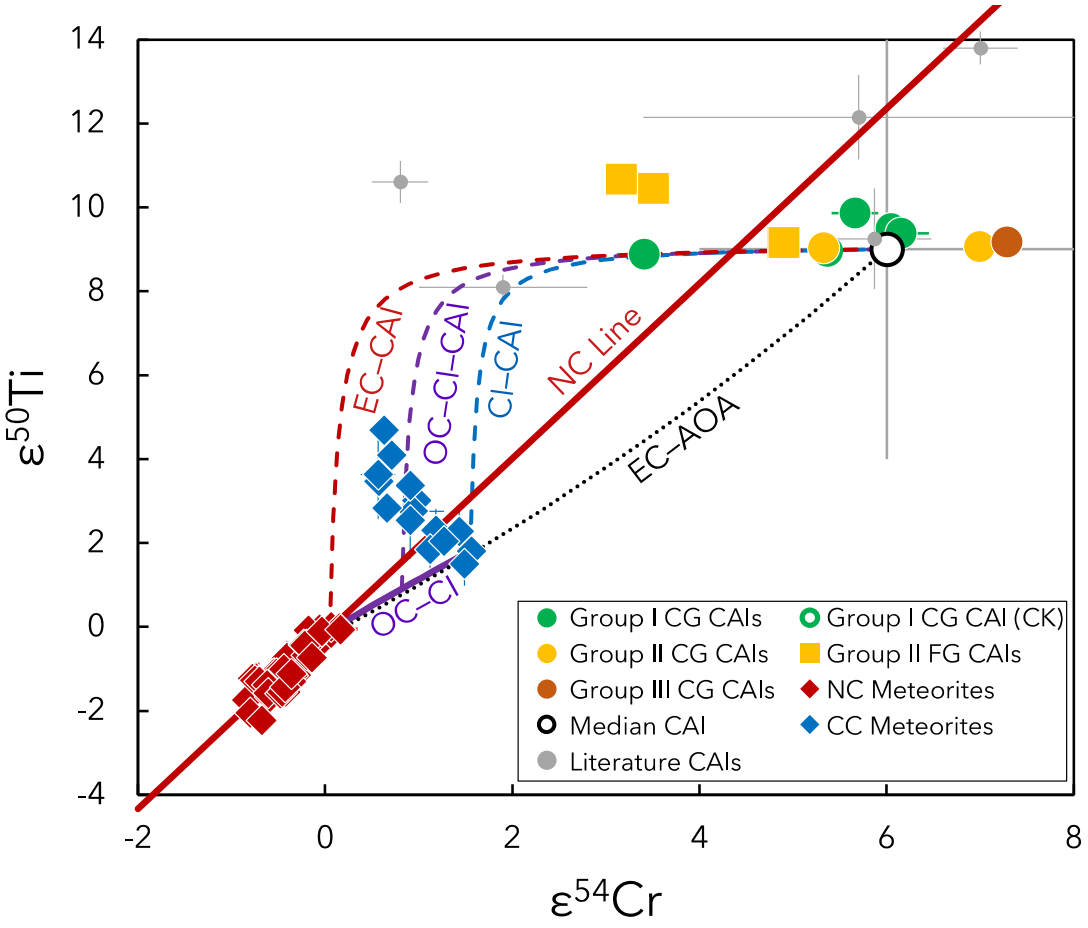

Fig. 10. ε^{50}Ti vs. ε^{54}Cr for CAIs studied here (colored circles and squares) and from the literature (solid gray circles) (Niederer et al., 1981; Papanastassiou, 1986; Loss et al., 1994), as well as for individual bulk NC and CC meteorites from the literature (red and blue diamonds, respectively; Shukolyukov and Lugmair, 2006; Trinquier et al., 2007, 2009; Qin et al., 2010; Zhang et al., 2012; Li et al., 2018; Torrano et al., 2019; Williams et al., 2020; Torrano et al., 2021; Zhu et al., 2021). The open black circle represents the median ε^{50}Ti and ε^{54}Cr values for all CAIs and AOAs studied here and in the literature, with 2SD error bars (from the data shown in Fig. 2 for CAIs and Trinquier et al., 2009 and Larsen et al., 2011 for AOAs). The solid red line represents a linear regression through the NC meteorite compositions, calculated using IsoplotR. Mixing lines are shown between the average composition of CAIs and enstatite chondrites (dashed red line), average AOAs and enstatite chondrites as modeled by Williams et al. (2020) (dotted black line), average CAIs and CI chondrites (dashed blue line), enstatite chondrites and CI chondrites (solid purple line), and average CAIs admixed with 70% CI chondrites/30% ordinary chondrites (dashed purple line). For the mixing line calculations, elemental concentrations for bulk meteorites are from the data compilations of Alexander et al. (2019a,b) and references therein, elemental concentrations

660 for CAIs are the mean concentrations of the CAIs studied here and in Torrano et al. (2019), and
661 elemental concentrations for AOAs are from Sugiura et al. (2009).
662

663 **5. CONCLUSIONS**

664 In this study, we report the mass-independent Cr and Ti isotopic compositions in a suite of
665 11 CAIs from six CV3 chondrites and one CK3 chondrite. The results and implications of this
666 work are summarized as follows:

667 1) The greater variability observed in ε^{54}Cr compared to ε^{50}Ti in CAIs is likely the result of
668 variable distribution of the distinct carrier phases of these isotopic anomalies and is not an
669 artifact resulting from matrix addition to the CAIs. It is also possible that thermal
670 processing in the disk affected these distinct carrier phases differently and this contributed
671 to the difference in variability of these two isotopes. Whereas the highest ε^{50}Ti values are
672 reported in fine-grained CAIs with fractionated group II REE patterns, these CAIs do not
673 have the highest ε^{54}Cr values. There is no clear correlation between isotopic compositions
674 and the degree of fractionation of the REE patterns of the CAIs. This suggests that the
675 processes leading to the isotopic anomalies observed in CAIs were distinct from the
676 processes responsible for the observed REE patterns.
677 2) The ε^{50}Ti isotopic compositions of CAIs define a narrow range and significant peak near
678 the median value when compared to the populations of other early-formed refractory
679 inclusions such as PLACs and SHIBs that have wider ranges but similar peaks near that of
680 CAIs. The progressively smaller isotopic range of ε^{50}Ti values in these progressively larger
681 refractory inclusions (i.e., isotopic range in PLACs > SHIBs > CAIs) and the similar
682 median ε^{50}Ti values for each of these populations suggests that the ε^{50}Ti compositions
683 recorded by CAIs likely record the mixing of the more isotopically anomalous PLACs and
684 SHIBs and the resulting greater degrees of homogenization and averaging of their isotopic
685 anomalies. This trend may also extend to presolar grains, which have even larger isotopic
686 anomalies. The progression of decreasing isotopic anomalies with increasing size from
687 presolar grains to PLACs, then to SHIBs, and finally to CAIs likely records the averaging
688 effect as isotopically anomalous inclusions combined to form progressively larger solids
689 in the protoplanetary disk.
690 3) We observe greater variability in both ε^{50}Ti and ε^{54}Cr values in smaller CAIs, while larger
691 CAIs exhibit ε^{50}Ti and ε^{54}Cr values that converge towards the median CAI isotopic

compositions. This additionally suggests that physical mixing of smaller carrier phase grains with larger and more variable isotopic anomalies create an averaging effect as an increasing number of these grains are combined to form larger CAIs.

4) CAIs and bulk meteorites define a correlation between ε^{46}Ti and ε^{50}Ti that does not extend to all PLACs and SHIBs, although PLACs and SHIBs with smaller isotopic anomalies plot closer to the CAI correlation line. This provides further evidence that the averaging of the isotopic compositions of these objects may be responsible for the isotopic compositions of CAIs. The Ti isotopic compositions of CAIs and bulk meteorites imply mixing between at least three distinct isotopic reservoirs that were present in the early Solar System since ^{46}Ti and ^{50}Ti are produced by different nucleosynthetic sources such as SNII, SNIa, and ECSN. The CAIs studied here exhibit an anti-correlation between $\varepsilon^{53}Cr_c$ and ε^{54}Cr, which suggests that the nucleosynthetic sources of the Cr carrier phases in CAIs are SNIa and/or ECSN rather than SNII.

5) The offset of the CC isotopic reservoir from the NC isotopic reservoir towards the isotopic composition of CAIs in ε^{50}Ti vs. ε^{54}Cr space cannot be solely from the addition of CAIs to a reservoir with NC composition. CAIs may record the isotopic composition of the earliest infalling material inherited by our protoplanetary disk (enriched in supernova-derived isotopes such as ε^{50}Ti and ^{54}Cr) and thus are likely to be one of the key components that were admixed to the NC composition to produce at least some of the range of CC isotopic compositions. Nevertheless, at least one other component such as AOAs or ^{54}Cr-enriched solids are required to account for the range of CC meteorite compositions.

Acknowledgments: We thank the Buseck Center for Meteorite Studies at ASU for providing the CAI samples studied here. We are especially grateful to Laurence Garvie for his assistance with the selection and acquisition of the samples from which these CAIs were obtained.

Funding: This work was supported by NASA grant NNX15AH41G to M. W. The contributions of G. A. B. to this study were performed under the auspices of the US DOE by Lawrence Livermore National Laboratory under Contract DE-AC52-07NA27344 with release number LLNL-JRNL-836804.

REFERENCES

Alexander C. M. O'D. (2019a) Quantitative models for the elemental and isotopic fractionations in chondrites: The carbonaceous chondrites. *Geochim. Cosmochim. Acta* **254**, 277–309.

Alexander C. M. O'D. (2019b) Quantitative models for the elemental and isotopic fractionations in the chondrites: The non-carbonaceous chondrites. *Geochim. Cosmochim. Acta* **254**, 246–276.

Alexander C. M. O'D. and Nittler L. R. (1999) The galactic evolution of Si, Ti, and O isotopic ratios. *Astrophys. J.* **519**, 222–235.

Amari S., Nittler L. R., Zinner E., Gallino R., Lugaro M. and Lewis R. S. (2001a) Presolar SiC grains of type Y: origin from low-metallicity asymptotic giant branch stars. *Astrophys. J.* **546**, 248–266.

Amari S., Nittler L. R., Zinner E., Lodders K. and Lewis R. S. (2001b) Presolar SiC grains of type A and B: their isotopic compositions and stellar origins. *Astrophys. J.* **559**, 463–483.

Amelin Y., Kaltenbach A., Iizuka T., Stirling C. H., Ireland T. R., Petaev M. and Jacobsen S. B. (2010) U-Pb chronology of the Solar System's oldest solids with variable $^{238}U/^{235}U$. *Earth Planet. Sci. Lett.* **300**, 343–350.

Birck J.-L. and Allègre C. J. (1984) Chromium isotopic anomalies in Allende Refractory Inclusions. *Geophys. Res. Lett.* **11**, 943–946.

Birck J.-L. and Allègre C. J. (1985) Evidence for the presence of ^{53}Mn in the early solar system. *Geophys. Res. Lett.* **12**, 745–748.

Birck J.-L. and Lugmair G. W. (1988) Nickel and chromium isotopes in Allende inclusions. *Earth Planet. Sci. Lett.* **90**, 131–143.

Bizzarro M., Baker J., and Haack H. (2004) Mg isotope evidence for contemporaneous formation of chondrules and refractory inclusions. *Nature* **431**, 275-278.

Boynton W. V. (1975) Fractionation in the solar nebula: condensation of yttrium and the rare earth elements. *Geochim. Cosmochim. Acta* **39**, 569–584.

Brennecka G. A., Borg L. E. and Wadhwa M. (2013) Evidence for supernova injection into the solar nebula and the decoupling of r-process nucleosynthesis. *Proc. Natl. Acad. Sci. U. S. A.* 110, 17241–17246.

Brennecka G. A., Burkhardt C., Budde G., Kruijer T. S., Nimmo F., Kleine T. (2020) Astronomical context of Solar System formation from molybdenum isotopes in meteorite inclusions.

754 *Science*. **370**, 837–840.
755 Bryson J. F. J. and Brennecka G. A. (2021) Constraints on chondrule generation, disk dynamics,
756 and asteroid accretion from the compositions of carbonaceous meteorites. *Astrophys. J.* **912**,
757 163.
758 Burkhardt C., Dauphas N., Hans U., Bourdon B. and Kleine T. (2019) Elemental and isotopic
759 variability in solar system materials by mixing and processing of primordial disk reservoirs.
760 *Geochim. Cosmochim. Acta* **261**, 145–170.
761 Chen H., Lee T., Lee D. and Iizuka Y. (2009) In situ Ti isotopic measurements by laser ablation
762 MC-ICP-MS. *Terr. Atmos. Ocean. Sci.* **20**, 703–712.
763 Ciesla F. J. (2010) The distributions and ages of refractory objects in the solar nebula. *Icarus*
764 **208**, 455–467.
765 Dauphas N., Remusat L., Chen J. H., Roskosz M., Papanastassiou D. A., Stodolna J., Guan Y., Ma
766 C. and Eiler J. M. (2010) Neutron-rich chromium isotope anomalies in supernova
767 nanoparticles. *Astrophys. J.* **720**, 1577–1591.
768 Dauphas N. and Schauble E. A. (2016) Mass fractionation laws, mass-independent effects, and
769 isotopic anomalies. *Annu. Rev. Earth Planet. Sci* **44**, 709–83.
770 Davis A. M. and Grossman L. (1979) Condensation and fractionation of rare earths in the solar
771 nebula. *Geochim. Cosmochim. Acta* **43**, 1611–1632.
772 Davis A. M., Zhang J., Greber N. D., Hu J., Tissot, F. L. H., Dauphas, N. (2018) Titanium
773 isotopes and rare earth patterns in CAIs: Evidence for thermal processing and gas-dust
774 decoupling in the protoplanetary disk. *Geochim. Cosmochim. Acta* **221**, 275–295.
775 Ebert S., Render J., Brennecka G. A., Burkhardt C., Bischoff A., Gerber S. and Kleine T. (2018)
776 Ti isotopic evidence for a non-CAI refractory component in the inner Solar System. *Earth*
777 *Planet. Sci. Lett.* **498**, 257–265.
778 Gerber S., Burkhardt C., Budde G., Metzler K. and Kleine T. (2017) Mixing and transport of
779 dust in the early solar nebula as inferred from titanium isotope variations among chondrules.
780 *Astrophys. J. Lett.* **841**, L17.
781 Göpel C., Birck J.-L., Galy A., Barrat J,-A., and Zanda B. (2015) Mn-Cr systematics in primitive
782 meteorites: insights from mineral separation and partial dissolution. *Geochim. Cosmochim.*
783 *Acta* **156**, 1–24.

784 Gyngard F., Amari S., Zinner E. and Marhas K. K. (2018) Correlated silicon and titanium isotopic
785 compositions of presolar SiC grains from the Murchison CM2 chondrite. *Geochim.*
786 *Cosmochim. Acta* **221**, 145–161.
787 Heydegger H. R., Foster J. J. and Compston W. (1979) Evidence of a new isotopic anomaly from
788 titanium isotopic ratios in meteoric materials. *Nature* **278**, 704–707.
789 Hoppe P., Amari S., Zinner E., Ireland T. and Lewis R. S. (1994) Carbon, nitrogen, magnesium,
790 silicon, and titanium isotopic compositions of single interstellar silicon carbide grains from
791 the Murchison carbonaceous chondrite. *Astrophys. J.* **430**, 870– 890.
792 Hu J. Y., Dauphas N., Tissot F. L. H., Yokochi R., Ireland T. J., Zhang Z., Davis A. M., Ciesla F.
793 J., Grossman L., Charlier B. L. A., Roskosz M., Alp E. E., Hu M. Y. and Zhao J. (2021)
794 Heating events in the nascent solar system recorded by rare earth element isotopic
795 fractionation in refractory inclusions. *Sci. Adv.* **7**, eabc2962.
796 Huss G. R. and Smith J. B. (2007) Titanium isotopic compositions of well-characterized silicon
797 carbide grains from Orgueil (CI): implications for s-process nucleosynthesis. *Meteorit.*
798 *Planet. Sci.* **42**, 1055–1075.
799 Ireland T. R. (1988) Correlated morphological, chemical, and isotopic characteristics of
800 hibonites from the Murchison carbonaceous chondrite. *Geochim. Cosmochim. Acta* **52**,
801 2827–2839.
802 Ireland T. R. (1990) Presolar isotopic and chemical signatures in hibonite-bearing refractory
803 inclusions from the Murchison carbonaceous chondrite. *Geochim. Cosmochim. Acta* **54**,
804 3219–3237.
805 Ireland T. R., Zinner E. K. and Amari S. (1991) Isotopically anomalous Ti in presolar SiC from
806 the Murchison meteorite. *Astrophys. J.* **376**, L53–L56.
807 Jacobsen B., Yin Q., Moynier F., Amelin Y., Krot A. N., Nagashima K., Hutcheon I. D. and
808 Palme H. (2008) ^{26}Al-^{26}Mg and ^{207}Pb-^{206}Pb systematics of Allende CAIs: canonical solar
809 initial ^{26}Al/^{27}Al ratio reinstated. *Geochim. Cosmochim. Acta* **272**, 353–364.
810 Jacquet E., Pignatale F. C., Chaussidon M. and Charnoz S. (2019) Fingerprints of the protosolar
811 cloud collapse in the solar Ssstem. II. Nucleosynthetic anomalies in meteorites. *Astrophys. J.*
812 **884**, 32, 11 pp.

Kawasaki N., Park C., Sakamoto N., Park S. Y., Kim H. N., Kuroda M. and Yurimoto H. (2019) Variations in initial $^{26}Al/^{27}Al$ ratios among fluffy Type A Ca–Al-rich inclusions from reduced CV chondrites. *Earth Planet. Sci. Lett.* **511**, 25–35.

Kööp L., Davis A. M., Nakashima D., Park C., Krot A. N., Nagashima K., Tenner T. J., Heck P. R. and Kita N. T. (2016a) A link between oxygen, calcium and titanium isotopes in ^{26}Al-poor hibonite-rich CAIs from Murchison and implications for the heterogeneity of dust reservoirs in the solar nebula. *Geochim. Cosmochim. Acta* **189** (70–95).

Kööp L., Nakashima D., Heck P. R., Kita N. T., Tenner T. J., Krot A. N., Nagashima K., Park C. and Davis A. M. (2016b) New constraints on the relationship between 26Al and oxygen, calcium, and titanium isotopic variation in the early Solar System from a multielement isotopic study of spinel-hibonite inclusions. Geochim. Cosmochim. Acta 184, 151–172.

Kööp L., Nagashima K., Kööp L., Nagashima K., Davis A. M. and Krot A. N. (2020) A refractory inclusion with solar oxygen isotopes and the rarity of such objects in the meteorite record. *Meteorit. Planet. Sci.* 1–11.

Krot A. N., Petaev M. I., Scott E. R. D., Choi B.-G., Zolensky M. E. and Keil K. (1998) Progressive alteration in CV3 chondrites: more evidence for asteroidal alteration. *Meteorit. Planet. Sci.* **33**, 748–775.

Krot A. N., Petaev M. I., Russell S. S., Itoh S., Fagan T. J., Yurimoto H., Chizmadia L., Weisberg M. K., Komatsu M., Ulyanov A. A. and Keil K. (2004) Amoeboid olivine aggregates and related objects in carbonaceous chondrites: Records of nebular and asteroid processes. *Chemie der Erde* **64**, 185–239.

Kruijer T. S., Burkhardt C., Budde G. and Kleine T. (2017) Age of Jupiter inferred from the distinct genetics and formation times of meteorites. *Proc. Natl. Acad. Sci.* **114**, 6712–6716.

Kruijer T. S., Kleine T. and Borg L. E. (2020) The great isotopic dichotomy of the early Solar System. *Nat. Astron.* **4**, 32–40.

Langbroek M., Jenniskens P., Kriegsman L. M., Nieuwenhuis H., De Kort N., Kuiper J., Van Westrenen W., Zolensky M. E., Ziegler and Yin Q. Z. (2019) The CM carbonaceous chondrite regolith Diepenveen. *Meteorit. Planet. Sci.* **54**, 1431–1461.

Larsen K. K., Trinquier A., Paton C., Schiller M., Wielandt D., Ivanova M. A., Connelly J. N., Nordlund A., Krot A. N. and Bizzarro M. (2011) Evidence for magnesium isotope hetero-geneity in the solar protoplanetary disk. *Astrophys. J. Lett.* **735**, L37.

Larsen K. K., Wielandt D., Schiller M. and Bizzarro M. (2016) Chromatographic speciation of Cr(III)-species, inter-species equilibrium isotope fractionation and improved chemical purification strategies for high-precision isotope analysis. *J. Chromatogr. A* **1443**, 162–174.

Leya I., Schönbächler M., Krähenbühl U. and Halliday A. N. (2009) New titanium isotope data for Allende and Efremovka CAIs. *Astrophys. J.* **702**, 1118–1126.

Li S., Yin Q. Z., Bao H., Sanborn M. E., Irving A., Ziegler K., Agee C., Marti K., Miao B., Li X., Li Y., Wang S. (2018) Evidence for a multilayered internal structure of the chondritic acapulcoite-lodranite parent asteroid. *Geochim. Cosmochim. Acta* **242**, 82–101.

Liu M.-C., McKeegan K. D., Goswami J. N., Marhas K. K., Sahijpal S., Ireland T. R. and Davis A. M. (2009) Isotopic records in CM hibonites: implications for timescales of mixing of isotope reservoirs in the solar nebula. *Geochim. Cosmochim. Acta* **73**, 5051–5079.

Liu M.-C., Han J., Brearley A. J. and Hertwig A. T. (2019) Aluminum-26 chronology of dust coagulation and early solar system evolution. *Sci. Adv.* **5**, 1–9.

Lodders K. (2003) Solar System abundances and condensation temperatures of the elements. *Astrophys. J.* **591**, 1220–1247.

Loss R. D., Lugmair G. W., Davis A. M. and MacPherson G. J. (1994) Isotopically distinct reservoirs in the solar nebula: isotope anomalies in Vigarano meteorite inclusions. *Astrophys. J.* **436**, L193–L196.

MacPherson G. J. and Davis A. M. (1994) Refractory inclusions in the prototypical CM chondrite, Mighei. *Geochim. Cosmochim. Acta* **58**, 5599–5625

MacPherson G. J., Kita N. T., Ushikubo T., Bullock E. S. and Davis A. M. (2012) Well-resolved variations in the formation ages for Ca-Al-rich inclusions in the early Solar System. *Earth Planet. Sci. Lett.* **331-332**, 43–54.

MacPherson G. J. (2014) Calcium-aluminum-rich inclusions in chondritic meteorites. In *Meteorites and Cosmochemical Processes* (Ed. A. M. Davis), Vol. 1 *Treatise on Geochemistry, 2nd Ed.* (Exec. Eds. H. D. Holland and K. K. Turekian), Elsevier, Oxford, pp. 139–179.

Martin P. M. and Mason B. (1974) Major and trace elements in the Allende meteorite. *Nature* **249**, 333–334.

Mason B. and Martin P. M. (1977) Geochemical differences among components of the Allende meteorite. *Smithson. Contrib. Earth Sci.* (**19**), 84–95.

875 Mason B. and Taylor S. R. (1982) Inclusions in the Allende Meteorite. *Smithsonian*
876 *Contributions to the Earth Sciences*. 1–30.
877 McKeegan K. D., Kallio A. P. A., Heber V. S., Jarzebinski G., Mao P. H., Coath C. D., Kunihiro
878 T., Wiens R. C., Nordholt J. E., Moses R. W., Reisenfeld D. B., Jurewicz A. J. G. and
879 Burnett D. S. (2011) The oxygen isotopic composition of the Sun inferred from captured
880 solar wind. *Science* **332**, 1528–1532.
881 Mougel B., Moynier F., Koeberl C., Wielandt D. and Bizzarro M. (2019) Identification of a
882 meteoritic component using chromium isotopic composition of impact rocks from the Lonar
883 impact structure, India. *Meteorit. Planet. Sci.* **54**, 2592– 2599.
884 Nanne J. A. M., Nimmo F., Cuzzi J. N. and Kleine T. (2019) Origin of the non-carbonaceous –
885 carbonaceous meteorite dichotomy. *Earth Planet. Sci. Lett.* **511**, 44–54.
886 Niederer F. R., Papanastassiou D. A. and Wasserburg G. J. (1980) Endemic isotopic anomalies
887 in titanium. *Astrophys. J.* **240**, L73–L77.
888 Niederer F. R., Papanastassiou D. A. and Wasserburg G. J. (1981) The isotopic composition of
889 titanium in the Allende and Leoville meteorites. *Geochim. Cosmochim. Acta* **45**, 1017–
890 1031.
891 Niederer F. R., Papanastassiou D. A. and Wasserburg G. J. (1985) Absolute isotopic abundances
892 of Ti in meteorites. *Geochim. Cosmochim. Acta* **49**, 835–851.
893 Niemeyer S. and Lugmair G. W. (1981) Ubiquitous isotopic anomalies in Ti from normal
894 Allende inclusions. *Earth Planet. Sci. Lett.* **53**, 211–225.
895 Niemeyer S. and Lugmair G. W. (1984) Titanium isotopic anomalies in meteorites. *Geochim.*
896 *Cosmochim. Acta* **48**, 1401–1416.
897 Niemeyer S. (1985) Systematics of Ti isotopes in carbonaceous chondrite whole-rock samples.
898 *Geophys. Res. Lett.* **12**, 733–736.
899 Niemeyer S. (1988) Titanium isotopic anomalies in chondrules from carbonaceous chondrites.
900 *Geochim. Cosmochim. Acta* **52**, 309–318.
901 Nittler L. R., Alexander C. M. O'D., Liu N. and Wang J. (2018) Extremely ^{54}Cr- and ^{50}Ti-rich
902 Presolar Oxide Grains in a Primitive Meteorite: Formation in Rare Types of Supernovae and
903 Implications for the Astrophysical Context of Solar System Birth. *Astrophys. J. Lett.* **856**,
904 L24.

905 Papanastassiou D. A. (1986) Chromium Isotopic Anomalies in the Allende Meteorite. *Astrophys.*
906 *J.* **308**, 27–30.
907 Papanastassiou D. A. and Brigham C. A. (1989) The identification of meteorite inclusions with
908 isotope anomalies. *Astrophys. J.* **338**, L37–40.
909 Pedersen S. G., Schiller M., Connelly J. N. and Bizzarro M. (2019) Testing accretion
910 mechanisms of the H chondrite parent body utilizing nucleosynthetic anomalies. *Meteorit.*
911 *Planet. Sci.* **54**, 1215–1227.
912 Qin L., Alexander C. M. O'D., Carlson R. W., Horan M. F. and Yokoyama T. (2010)
913 Contributors to chromium isotope variation of meteorites. *Geochim. Cosmochim. Acta* **74**,
914 1122–1145.
915 Qin L., Nittler L. R., Alexander C. M. O'D., Wang J., Stadermann F. J. and Carlson R. W.
916 (2011) Extreme ^{54}Cr-rich nano-oxides in the CI chondrite Orgueil – Implication for a late
917 supernova injection into the solar system. *Geochim. Cosmochim. Acta* **75**, 629–644.
918 Rauscher T., Heger A., Hoffman R. D. and Woosley S. E. (2002) Nucleosynthesis in massive
919 stars with improved nuclear and stellar physics. *Astrophys. J.* **576**, 323–348.
920 Render J., Brennecka G. A., Wang S.-J., Wasylenki L. E. and Kleine T. (2018) A Distinct
921 Nucleosynthetic Heritage for Early Solar System Solids Recorded by Ni Isotope Signatures.
922 *Astrophys. J.* **862**, 26–43.
923 Render J., Ebert S., Burkhardt C., Kleine T. and Brennecka G. A. (2019) Titanium isotopic
924 evidence for a shared genetic heritage of refractory inclusions from different carbonaceous
925 chondrites. *Geochim. Cosmochim. Acta* **254**, 40–53.
926 Ruzicka A., Floss C. and Hutson M. (2012) Amoeboid olivine aggregates (AOAs) in the
927 Efremovka, Leoville and Vigarano (CV3) chondrites: A record of condensate evolution in
928 the solar nebula. *Geochim. Cosmochim. Acta* **79**, 79–105.
929 Sahijpal S. and Goswami J. N. (1998) Refractory phases in primitive meteorites devoid of 26Al
930 and 41Ca: representative samples of first solar system solids? *Astrophys. J.* 509, L137–
931 L140.
932 Sahijpal S., Goswami J. N. and Davis A. M. (2000) K, Mg, Ti and Ca isotopic compositions and
933 refractory trace element abun- dances in hibonites from CM and CV meteorites:
934 Implications for early solar system processes. *Geochim. Cosmochim. Acta* **64**, 1989–2005.
935 Sanborn M. E., Wimpenny J., Williams C. D., Yamakawa A., Amelin Y., Irving A. J. and Yin Q.

936 Z. (2019) Carbonaceous achondrites Northwest Africa 6704/6693: Milestones for early
937 Solar System chronology and genealogy. *Geochim. Cosmochim. Acta* **245**, 577–596.
938 Schiller M., Van Kooten E., Holst J. C., Olsen M. B. and Bizzarro M. (2014) Precise measurement
939 of chromium isotopes by MC- ICPMS. *J. Anal. At. Spectrom.* **29**, 1406–1416.
940 Schneider J. M., Burkhardt C., Marrocchi Y., Brennecka G. A. and Kleine T. (2020) Early
941 evolution of the solar accretion disk inferred from Cr-Ti-O isotopes in individual
942 chondrules. *Earth Planet. Sci. Lett.* **551**, 116585.
943 Shields W. R., Murphy J. T., Cantazaro E. J. and Garner E. L. (1966) Absolute isotopic
944 abundance ratios and the atomic weight of a reference sample of chromium. *J. Res. Natl.*
945 *Bur. Stand*. 70A, 193–197.
946 Shollenberger, Q. R., Render, J., Jordan, M. K., McCain, K. A., Ebert, S., Bischoff, A., Kleine,
947 T., Young, E. D. (2022) Titanium isotope systematics of refractory inclusions: Echoes of
948 molecular cloud heterogeneity. *Geochim. Cosmochim. Acta* **324**, 44–65.
949 Shukolyukov A., and Lugmair G. W. (2006) Manganese-chromium isotope systematics of
950 carbonaceous chondrites. *Earth Planet. Sci. Lett.*, **250**, 200–213.
951 Simon J. I., Jordan M. K., Tappa M. J., Schauble E. A., Kohl I. E. and Young E. D. (2017)
952 Calcium and titanium isotope fractionation in refractory inclusions: tracers of condensation
953 and inheritance in the early solar protoplanetary disk. *Earth Planet. Sci. Lett*. **472**, 277–288.
954 Sugiura N., Petaev M. I., Kimura M., Miyazaki A. and Hiyagon H. (2009) Nebular history of
955 amoeboid olivine aggregates. *Meteorit. Planet. Sci.* **44**, 559–572.
956 Tissot F. L. H., Dauphas N. and Grove T. L. (2017) Distinct $^{238}U/^{235}U$ ratios and REE patterns in
957 plutonic and volcanic angrites: Geochronologic implications and evidence for U isotope
958 fractionation during magmatic processes. *Geochim. Cosmochim. Acta* **213**, 593–617.
959 Torrano Z. A., Brennecka G. A., Williams C. D., Romaniello S. J., Rai V. K., Hines R. R. and
960 Wadhwa M. (2019) Titanium isotope signatures of calcium-aluminum-rich inclusions from
961 CV and CK chondrites: Implications for early Solar System reservoirs and mixing.
962 *Geochim. Cosmochim. Acta* **263**, 13–30.
963 Torrano Z. A., Davidson J. and Wadhwa M. (2020) A reclassification of Northwest Africa 2900
964 from CV3 to CK3 chondrite. *Meteorit Planet Sci*, **55**, 2539–2550.
965 Torrano Z. A., Schrader D. L., Davidson J., Greenwood R. C., Dunlap D. R., Wadhwa M. (2021)
966 The relationship between CM and CO chondrites: Insights from combined analyses of

967 titanium, chromium, and oxygen isotopes in CM, CO, and ungrouped chondrites.
968 *Geochimica et Cosmochimica Acta* (Accepted)
969 Trinquier A., Birck J.-L. and Allègre C. J. (2007) Widespread ^{54}Cr Heterogeneity in the Inner
970 Solar System. *Astrophys. J.* **655**, 1179–1185.
971 Trinquier A., Birck J.-L., Allègre C. J., Göpel C. and Ulfbeck D. (2008) ^{53}Mn-^{53}Cr systematics
972 of the early Solar System revisited. *Geochim. Cosmochim. Acta* **72**, 5146–5163.
973 Trinquier A., Elliott T., Ulfbeck D., Coath C., Krot A. N. and Bizzarro M. (2009) Origin of
974 nucleosynthetic isotope heterogeneity in the solar protoplanetary disk. *Science* **324**, 374–376.
975 Van Kooten E., Cavalcante L., Wielandt D. and Bizzarro M. (2020), The role of Bells in the
976 continuous accretion between the CM and CR chondrite reservoirs. *Meteorit Planet Sci*, **55**,
977 575–590.
978 Wanajo S., Janka H. T. and Müller B. (2013) Electron-capture supernovae as origin of ^{48}Ca.
979 *Astrophys. J. Lett.* **767**, L26, 6 pp.
980 Warren P. H. (2011) Stable-isotopic anomalies and the accretionary assemblage of the Earth and
981 Mars: A subordinate role for carbonaceous chondrites. *Earth Planet. Sci. Lett.* **311**, 93–100.
982 Weisberg M. K., McCoy T. J., and Krot A. N. (2006) Systematics and evaluation of meteorite
983 classification. *Meteorites and the early solar system, 2nd ed.,* edited by Lauretta D. S. and
984 McSween H. Y. Jr. Tucson, Arizona: The University of Arizona Press. 19–52.
985 Williams C. D., Janney P. E., Hines R. R. and Wadhwa M. (2016) Precise titanium isotope
986 compositions of refractory inclusions in the Allende CV3 chondrite by LA-MC-ICPMS.
987 *Chem. Geol.* **436**, 1–10.
988 Williams C. D., Sanborn M. E., Defouilloy C., Yin Q.-Z., Kita N. T., Ebel D. S., Yamakawa A.
989 and Yamashita K. (2020) Chondrules reveal large-scale outward transport of inner Solar
990 System materials in the protoplanetary disk. *Proc. Natl. Acad. Sci.* **117**, 23426–23435.
991 Wood J. A. (2004) Formation of chondritic refractory inclusions: the astrophysical setting.
992 *Geochim. Cosmochim. Acta* **68**, 4007–4021.
993 Woosley S. E. (1997) Neutron-rich Nucleosynthesis in Carbon Deflagration Supernovae.
994 *Astrophys. J.* **476**, 801–810.
995 Woosley S. E., Heger A. and Weaver T. A. (2002) The evolution and explosion of massive stars.
996 *Rev. Modern Phys.* **74**, 1015–1071.

997 Yamakawa A., Yamashita K., Makishima A., and Nakamura E. (2010) Chromium isotope
998 systematics of achondrites: Chronology and isotopic heterogeneity of the inner solar system
999 bodies. *Astrophys. J.* **720**, 150–154.
1000 Yang L. and Ciesla F. J. (2012) The effects of disk building on the distributions of refractory
1001 materials in the solar nebula. *Meteorit. Planet. Sci.* **47**, 99–119.
1002 Zhang J., Dauphas N., Davis A. M. and Pourmand A. (2011) A new method for MC-ICPMS
1003 measurement of titanium isotopic composition: Identification of correlated isotope
1004 anomalies in meteorites. *J. Anal. At. Spectrom.* **26**, 2197-2205.
1005 Zhang J., Dauphas N., Davis A. M., Leya I. and Fedkin A. (2012) The proto-Earth as a
1006 significant source of lunar material. *Nature Geosci.* **5,** 251–255.
1007 Zhu K., Moynier F., Schiller M., Alexander C. M. O'D., Davidson J., Schrader D. L., van
1008 Kooten E., and Bizzarro M. (2021) Chromium isotopic insights into the origin of chondrite
1009 parent bodies and the early terrestrial volatile depletion. *Geochimica et Cosmochimica Acta*
1010 **301,** 158–186.
1011 Zinner E., Amari S., Guinness R., Jennings C., Mertz A. F., Nguyen A. N., Gallino R., Hoppe P.,
1012 Lugaro M., Nittler L. R. and Lewis R. S. (2007) NanoSIMS isotopic analysis of small
1013 presolar grains: search for Si3N4 grains from AGB stars, and Al and Ti isotopic
1014 compositions of rare presolar SiC grains. *Geochem. Cosmochim. Acta* **71**, 4786–4813.